

## Calibration for discrete element modelling of railway ballast

### A review

Guo, Yunlong; Zhao, Chunfa; Markine, Valeri; Jing, Guoqing; Zhai, Wanming

#### DOI

[10.1016/j.trgeo.2020.100341](https://doi.org/10.1016/j.trgeo.2020.100341)

#### Publication date

2020

#### Document Version

Accepted author manuscript

#### Published in

Transportation Geotechnics

#### Citation (APA)

Guo, Y., Zhao, C., Markine, V., Jing, G., & Zhai, W. (2020). Calibration for discrete element modelling of railway ballast: A review. *Transportation Geotechnics*, 23, Article 100341. <https://doi.org/10.1016/j.trgeo.2020.100341>

#### Important note

To cite this publication, please use the final published version (if applicable). Please check the document version above.

#### Copyright

Other than for strictly personal use, it is not permitted to download, forward or distribute the text or part of it, without the consent of the author(s) and/or copyright holder(s), unless the work is under an open content license such as Creative Commons.

#### Takedown policy

Please contact us and provide details if you believe this document breaches copyrights. We will remove access to the work immediately and investigate your claim.

# 1 Calibration for discrete element 2 modelling of railway ballast: A review

---

3 Yunlong Guo<sup>1</sup>, Chunfa Zhao<sup>2</sup>, Valeri Markine<sup>1</sup>, Guoqing Jing<sup>3</sup>, Wanming Zhai<sup>2\*</sup>

4 1. Faculty of Civil Engineering and Geosciences, Delft University of Technology, Delft, 2628CN,  
5 Netherlands

6 2. Train and Track Research Institute, National Traction Power Laboratory, Southwest Jiaotong  
7 University, Chengdu, 610031, China

8 3. School of Civil Engineering, Beijing Jiaotong University, Beijing, 100044, China

9 \*. Corresponding author

10 Email addresses: [yunlong.guo@tudelft.nl](mailto:yunlong.guo@tudelft.nl) (Y. Guo); [cfzhao@swjtu.edu.cn](mailto:cfzhao@swjtu.edu.cn) (C. Zhao);  
11 [v.l.markine@tudelft.nl](mailto:v.l.markine@tudelft.nl) (V. Markine); [gqjing@bjtu.edu.cn](mailto:gqjing@bjtu.edu.cn) (G. Jing); [wmzhai@swjtu.edu.cn](mailto:wmzhai@swjtu.edu.cn) (W. Zhai)

12

13 **Abstract:** The discrete element method (DEM) has been confirmed as an effective numerical method  
14 for modelling railway ballast, and successfully used to analyse a wide range of ballast-related  
15 applications (e.g. geomaterials). However, there still exists some aspects under development. Among  
16 them, the model calibration can be the most significant one (morphology, degradation and contact  
17 model). Because reliable and accurate results can be obtained only when the parameters are  
18 carefully selected. Therefore, diverse DEM applications and developments in railway ballast are  
19 critically reviewed. Furthermore, the model calibration methods are discussed. This is able to help  
20 future researchers improve the existing calibration methods, further, build more accurate,  
21 standardised and validated DEM models for ballast-related studies. Additionally, this paper can assist  
22 researchers to choose an appropriate model for specific applications.

23 **Keywords:** discrete element method; ballast; calibration; degradation; particle shape; morphology;  
24 contact model

## 25 1. Introduction

26 Ballast bed is the largest component in a ballast track (by volume and weight), with the functions of  
27 supporting sleepers uniformly, transmitting loadings to the subgrade and providing sufficient  
28 drainage [1]. As undergoing complex conditions (weather, water, loading etc.), a wide range of  
29 research problems emerge for the ballast layer [2-4], such as:

- 30 • Performance evaluation: the performance characteristics of the ballast bed mainly contain  
31 durability, stability, shear strength, stiffness and resilience [5]. Nowadays, they can be analysed  
32 with the models of laboratory tests (e.g. direct shear test) or field tests (e.g. single sleeper push  
33 test, sleeper supporting condition).
- 34 • Ballast bed degradation mechanism: the mechanism of ballast bed degradation and the  
35 associated plastic deformations have not been revealed clearly, especially at some special  
36 railway structures, e.g. turnouts, transition zones. The problem becomes more complicated,  
37 due to the increasing train speed and heavier haul [4, 6].
- 38 • Ballast degradation mitigation and performance improvement: Using other materials in the  
39 ballast layer is an effective means for ballast degradation mitigation and performance  
40 improvement, e.g., using the under sleeper pads, geogrid, geocell, polyurethane [7], etc.
- 41 • Maintenance: frequent maintenance cycles are leading to increasingly expensive cost. More  
42 importantly, tamping (the most common maintenance) causes ballast particle degradation

43 (breakage and abrasion) due to the impact from the insertion of the tamping tines into the  
44 ballast and the high squeezing force.

45 To solve these problems, the discrete element method (DEM) is used in plenty of ballast-related  
46 studies and has been proved to be an effective numerical method [8-11]. The DEM is a numerical  
47 model or computer simulation approach that can simulate granular materials. It describes the  
48 mechanical behaviour of assemblies of spheres (discs in 2D) or polyhedrons (polygons in 2D) and  
49 considers the individual particles in granular materials and their interactions (e.g. contacts, motions)  
50 [12, 13]. Nowadays, it has become a powerful and efficient tool to reproduce the performance and  
51 deformation of granular materials [14]. Particularly, the DEM is widely applied in the ballast-related  
52 studies due to the advantage that an identical sample can be performed with various test conditions  
53 (e.g. loading). Moreover, using the DEM can perform some detailed parametric studies that are often  
54 not feasible in laboratory tests, e.g., interparticle friction and distribution of contact forces. More  
55 importantly, it can record the complete particle information (e.g. displacement, acceleration) during  
56 the numerical simulations, consider the characteristics of ballast particles (e.g. size, density), and  
57 understand the effects of ballast particle degradation (i.e. breakage and abrasion) on the  
58 performance and deformation of the ballast assemblies.

59 Regarding the above-mentioned research problems, the DEM has been effectively applied to study  
60 them. For instance, the performance evaluation of ballast assemblies under various conditions (e.g.  
61 particle size distribution, fouling/contamination) can be performed with the models of direct shear  
62 tests [15-22], ballast box test [10, 23-26] or the triaxial tests [27-35]. Alternatively, the performance  
63 evaluation can be analysed with the model of field tests, e.g., the single sleeper push test model [9,  
64 14, 36-39] and the in-situ ballast track model [8, 18, 40-50].

65 Concerning the degradation mechanism, both the ballast particle degradation and ballast bed  
66 degradation were collectively expressed as ballast degradation and in the earlier studies they were  
67 not clearly distinguished. Because of this, this paper utilises the ballast particle degradation to  
68 present the ballast breakage and abrasion, and the ballast bed degradation to present the plastic  
69 deformation or fouled ballast bed. The ballast degradation presents the combination of the ballast  
70 bed degradation and the ballast particle degradation. When considering the particle degradation in  
71 the DEM models, setting the breakage and abrasion criterions is the first step (explained in Section  
72 Ballast particle degradation) [27, 34, 41, 46, 51-54]. With the criterions, the corresponding plastic  
73 deformation or fouled ballast bed performance can be presented, e.g. [25, 42, 48, 55]. Particularly,  
74 the DEM models have also been applied in the dynamic performance and degradation study of  
75 ballast bed at the transition zone [11, 56].

76 As for the ballast degradation mitigation and performance improvement, the under sleeper pads [10],  
77 the geogrid [26, 29, 56-63], the geocell [64, 65] and the polyurethane [7, 66] are the widely-used  
78 geomaterials. Plenty of studies with DEM models have been performed to demonstrate their  
79 effectiveness and propose application advices.

80 Regarding the track maintenance, tamping is the most common means operated on ballast layer to  
81 restore the track elastic and geometry. Using the DEM models, the studies mainly concern the  
82 tamping frequency, compaction and performance after tamping, etc. [38, 67-73].

83 From the above introduction, it can be seen that the DEM has been successfully applied for ballast-  
84 related studies and solved some of the research problems. However, when applying the DEM to the  
85 ballast-related studies, there still exists some unperfected aspects on the calibration, which may lead  
86 to inaccurate or even false results. Moreover, the computational cost is a general problem not only  
87 when a large ballast bed model is needed, but also when ballast particles are precisely built with the  
88 consideration of particle degradation.

89 In response to these limitations, this paper reviews the ballast-related studies using the DEM and  
90 summarises their calibration methods. The model calibration is to change the model characteristics

91 aiming to make the model more analogous to the real, and the characteristics primarily contain the  
92 morphology (shape and size), particle degradation (breakage and abrasion) and contact models.

93 Reviewing these DEM applications is helpful for researchers comparing and improving current  
94 models until the calibrated model with appropriate computational cost is built, further deepening  
95 their studies on the above-mentioned research problems.

96 Firstly, gathering all the knowledge in a single paper could offer researchers with the model  
97 comparison and a reliable argument. On one hand, this paper almost gathers all the DEM studies on  
98 ballast, and provides all their calibration means. By comparing them, the researchers can choose the  
99 proper calibration (model characteristics) means when building new type of models. On the other  
100 hand, this is beneficial for improving the model characteristics and parameters until they are verified  
101 and standardised, due to the proposed and applied ones in each model are various and have not  
102 reached a consensus.

103 Secondly, this can assist researchers to balance the time constraints and model precision when  
104 finding the solution to the above-mentioned research problems. Specifically, the gathered models  
105 contain precise models and the simplified ones, as well as their characteristics and parameters. The  
106 focused part could be built precisely, whereas the less concerned part could be built with simplified  
107 models. This can save large amount of the computational cost.

108 Lastly, this could help to show the developing trends and evolutions of the DEM, which is helpful for  
109 the beginners in this area to find a potential direction. More importantly, this could be helpful for the  
110 prediction of the next research hotspot.

## 111 2. Model calibration

112 The model calibration is to modify model characteristics to approach the real conditions, and the  
113 characteristics in the current studies mainly contain the morphology, particle degradation and  
114 contact model.

### 115 2.1. Morphology

116 Ballast particle morphology includes the particle shape and particle size, and it is a significant  
117 characteristic when building DEM models to study the performance of ballast assemblies. Because  
118 the particle morphology influences the packing, bulk density, contacts (coordination number),  
119 particle degradation and porosity [41, 74-76], which are critical factors influencing on the  
120 performance of ballast assemblies [16]. Consequently, in the standards for ballast [77-79], the  
121 morphology is required to meet some regulations. For instance, the particle size should be  
122 approximately in the range of 20 to 60 mm, and the grading should be within the lower and upper  
123 bands of the grading curve. Additionally, the ballast particles with the elongated or flaky shapes are  
124 also required to be less than some percentage (e.g. 10% in [78]).

#### 125 2.1.1. Shape

126 In early studies, the spheres (discs) were applied as ballast particles in the DEM models as shown in  
127 Table 1 (No. 1, 2). The discs/spheres are the basic element in the DEM at the beginning (proposed in  
128 [12]), because using spheres (discs) the contact detection is more efficient. However, the spheres  
129 (discs) cannot present the interlocks between ballast particles, furthermore, they cannot provide  
130 sufficient internal friction or shear strength [24, 80].

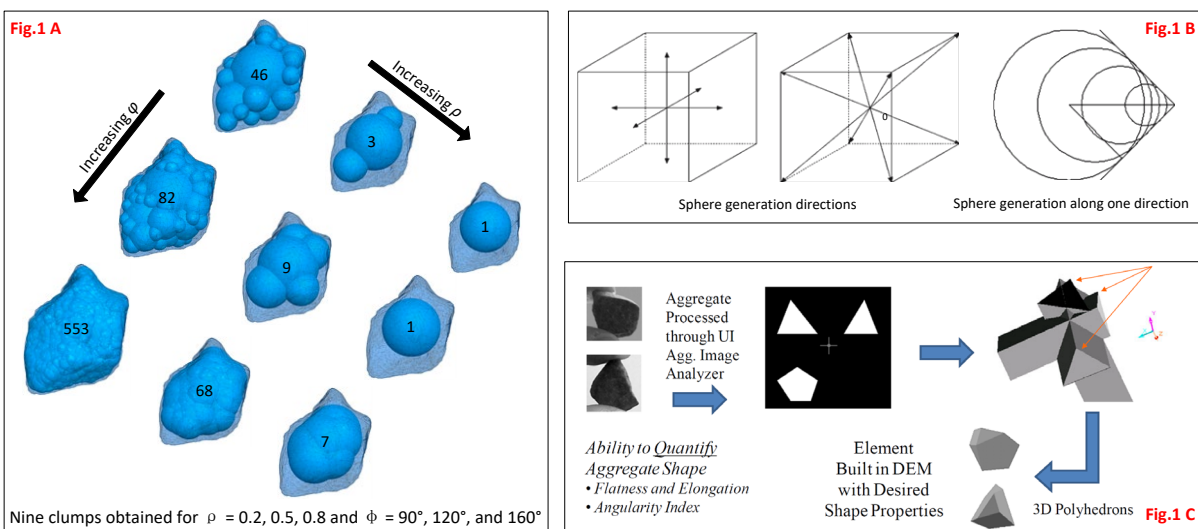
131 Towards this problem, two types of solutions are proposed. One is to change the basic element to  
132 the polyhedron (polygon) or spheropolyhedron, given in Table 1 (No. 16-18). The other is to improve  
133 the disc/sphere into assembly of spheres (agglomerate), i.e. Table 1 (No. 3-15). In most studies, the  
134 agglomerate contains three types, i.e. clump, cluster and clump & cluster (Table 1, No. 9). Table 1  
135 presents the shape calibration for ballast in the earlier studies, and it elucidates the basic element  
136 type, typical particle illustration, particle generation method and advantage & disadvantage.

137 Regarding the basic element, sphere (disc), polyhedron (polygon) and spheropolyhedron are included.  
 138 It needs to note that the agglomerates (clump, cluster, and clump & cluster) are built by using several  
 139 spheres (or discs) for one particle. The clump (a rigid body) cannot crush despite of the magnitude of  
 140 the loaded forces, whereas the cluster can crush due to the constituent spheres (discs) are bonded  
 141 together with the parallel bonds. The clusters are able to crush by parallel bond failure when the  
 142 acted force on them is over the prescribed value [81]. The combination of clump and cluster (clump  
 143 & cluster) is to bond spheres to the clump, and the bonded spheres can be released from the clump  
 144 as particle breakage. The polyhedron (polygon) is able to present the sharp edges and corners,  
 145 showing better shape and performance. The spheropolyhedron is an assembly of many shapes,  
 146 including the spheres, cubes, cylinders, etc.

147 Concerning the typical particle illustration, it means the typical particles utilised in the references and  
 148 their figures are illustrated. The figures are reproduced from the references given in the Column  
 149 Reference, by which the shape calibration is easier to explain visually. The following column is the  
 150 generation method, which describes the applied DEM software and the methods of creating the  
 151 particles. The applied software includes 1) particle flow code (PFC) [82], 2) Yade [83], 3) extended  
 152 discrete element method (EDEM), 4) dynamic optimization method [73], 5) BLOKS3D [84] and 6)  
 153 LMGC90 [85].

154 In the generation methods, various algorithms are applied to obtain different particle shapes. For the  
 155 basic element of spheres (discs), the clump or cluster with several spheres (discs) is initially built to  
 156 achieve the rough equilateral polyhedron (polygon), e.g. tetrahedron, cube (Table 1, No. 3, 4, 10, 15).  
 157 For making the shape more irregular with more realistic surface texture, angularity, more uniform  
 158 spheres (discs) are utilised to build one particle with the Hexagonal close packing (HCP) [53], e.g.  
 159 Table 1, No. 6, 7, 8, 12. Additionally, the particle shape is from various more advanced techniques  
 160 (3D image, digital image). However, more spheres (discs) considerably increase the computing time.  
 161 Towards this limitation, the algorithms are improved to reduce the sphere (disc) numbers by applying  
 162 large together with small spheres, e.g. Table 1, No. 5, 11, 13, 14. A detailed common example from  
 163 the PFC is shown in Figure 1A.

164 In this algorithm, two important parameters should be determined. One is  $\rho$ , the ratio of the smallest  
 165 to the largest sphere, and the other is  $\phi$ , the maximum sphere-sphere intersection angle [86]. The  
 166 two parameters decide the sphere number and the accuracy of the clump (Figure 1A). The figure also  
 167 presents the sphere numbers used to create the clump.





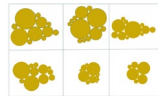
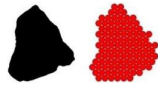
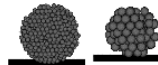
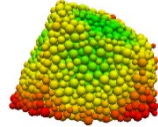
168  
 169 Figure 1 (A) clump generation method example; (B) Particle generation method in Table 1, No. 11; (C) Particle shape  
 170 determination method based on imaging (figures reproduced from [24, 60])

171 Some other algorithms are also given in Table 1, i.e. No. 9, 11, 12. The No. 9 presents a combination  
 172 of the clump and cluster, which applies the clump as the main body bonded with some asperities as

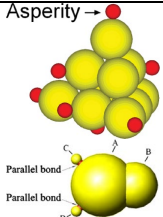
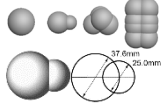
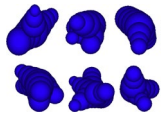
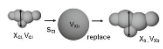
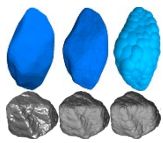
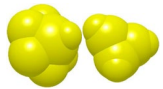
173 the corners. The No. 11 describes the algorithm allows overlapping sphere at 14 random directions,  
174 i.e. 6 faces and 8 corners, as shown in Figure 1B. The figure also presents the sphere generation along  
175 one direction.

176 For the basic element of polyhedron (polygon) or spheropolyhedron, the shape determination is an  
177 important part in the generation methods. The irregular shapes of BLOKS3D, LMGC90 and  
178 spheropolyhedron in [28, 33] (Table 1, No. 16, 17) are based on the photography of the real ballast  
179 particles, as shown in Figure 1C. Another method for irregular particle shape determination is applied  
180 in the No. 18, which utilises the Minkowski-Voronoi diagrams (explanations in [87]). Specifically, the  
181 Voronoi construction is decomposing a cube into separated convex polyhedrons, and the Minkowski  
182 operator is to dilate the convex polyhedrons as hemi-spherical vertices and edges.

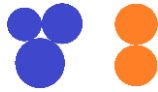
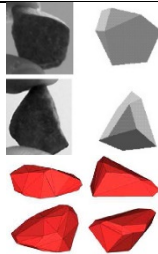


183 The last table column describes the advantages and disadvantages of each shape calibration method,  
184 as shown in Table 1. The advantages and disadvantages are discussed in four aspects, i.e. shape  
185 reality, computation cost, contact interlocking and performance. Moreover, the developments,  
186 discussions and highlights are also given in the column. The shape reality is defined as comparing the  
187 DEM particle shape with the real ballast particle shape. The computation cost means the computing  
188 time. The contact interlocking is the strength of the contacts between particles, which are mostly  
189 related with the performance of the whole ballast sample. The performance contains two aspects.  
190 One is the macroscopic appearance of the ballast sample in the laboratory or field tests, e.g. the  
191 deformation and shear strength. The other is the mesoscopic appearance of the ballast sample, e.g.  
192 the stress concentration [88].

No.	Reference	Type	Shape	Generation method	Advantage, disadvantage, highlight
1	Lobo-Guerrero [46, 89, 90]	Disc	-	PFC Basic element generation in the PFC.	Low computation cost; low shape reality; weak contact interlocking; two-dimensional with unrealistic settlement performance
2	Mahmud [59, 91]; Song [92]	Sphere	-	PFC (Mahmud); Yade (Song) Basic element generation in the software.	Low computation cost; low shape reality; weak contact interlocking; unrealistic performance (shear strength). Easy controlling the conditions, e.g. particle size distribution, porosity
3	Alaei [93]	Clump (discs)		PFC The discs are made into regular shape particles with small discs as corners.	Medium computation cost; medium shape reality; medium contact interlocking; two-dimensional with intermediately realistic performance (shear strength). After particle breakage, small discs can behave as fresh rough fracture surface.
4	Indraratna [54]	Cluster (discs)		PFC Bonding discs with parallel bonds and some of them are overlapped. Regular shape particles are generated with small discs as corners.	Medium computation cost; medium shape reality; medium contact interlocking; two-dimensional with intermediately realistic performance (shear strength). Crushable particle with small discs as angular, which can behave as angularity loss.
5	Indraratna [34, 44, 94]; Mahmoud [45]; Xiao [31]	Cluster (discs)		PFC Bonding discs with parallel bonds and no overlapped discs. Large and small discs are combined under user's definition to fit in the particle image cross sections.	Medium computation cost; medium shape reality; medium contact interlocking; two-dimensional with intermediately realistic performance (shear strength). Using the combination of big and small discs for disc number reduction per particle.
6	Zhang [8]; Mahmoud [45]	Cluster (discs; Mahmoud) Clump (discs; Zhang)		PFC Uniform discs filled in the particle image cross sections based on the HCP, and the discs are boned with parallel bonds to make cluster. The clump (Zhang) is a whole particle without bonds between discs.	High computation cost; medium shape reality; medium contact interlocking; two-dimensional with intermediately realistic performance (acceleration, settlement). The difference between the clump and the cluster is that the discs within each cluster also applies force-displacement cycles, which costs more time than the clump. But the cluster can break at random breakage types (e.g. break in the middle).
7	McDowell [95]; Qian [53]	Cluster (spheres)		PFC Uniform spheres are generated based on the HCP and bonded with parallel bonds.	High computation cost; medium shape reality; high contact interlocking; three-dimensional with realistic performance (settlement, single particle crushing).
8	Zhang [96]; Ergenzinger [97, 98]; Wang [51]	Cluster (spheres)		PFC Uniform spheres are filled in the geometry obtained from 3D image or self-defined shape and bonded with parallel bonds.	High computation cost; high shape reality; high contact interlocking; three-dimensional with realistic performance (settlement, single particle crushing). The particle has more realistic shape, but much higher computation cost.



9	McDowell [25, 27, 30, 80]	Clump & cluster (spheres)		<p>PFC</p> <p>The clump (overlapped or non-overlapped) is generated as main body with breakage asperities, simulated by bonding small spheres with parallel bonds.</p>	<p>Medium computation cost; medium shape reality; medium contact interlocking; three-dimensional with intermediately realistic performance (shear strength, repose angle, settlement). The ballast abrasion or sharp corner loss is reflected by losing the small spheres that are bonded by the parallel bond. No breakages are allowed in the other part.</p>
10	Mahmud [16, 41]; Gong [99]; Kumara [100]; Chen [26, 32, 56, 57]	Clump (spheres)		<p>PFC (Mahmud, Chen); Yade (Gong, Kumara)</p> <p>The clump is generated by using overlapped spheres, based on the researchers' design with regular shapes.</p>	<p>Medium computation cost; low shape reality; medium contact interlocking; three-dimensional with intermediately realistic performance (shear strength, lateral deformation, repose angle, settlement).</p>
11	Jing [17]; McDowell [24]	Clump (spheres)		<p>PFC</p> <p>The clump is generated by using overlapped spheres based on the developed algorithm. Specifically, a sphere is generated firstly. Afterwards, based on the sphere radius and coordinates, the sphere is replaced by a smaller sphere at the centre coordinates. Finally, the centre sphere is combined with several overlapped spheres generated at 4 random directions from 14 ones (Figure 1B).</p>	<p>Medium computation cost; medium shape reality; high contact interlocking; three-dimensional with intermediately realistic performance (deformation, shear strength). The particle is concave and the concave particles are uncrushable, inducing the possibility of stress concentration, thus reducing relative particle movements.</p>
12	Stahl [101]	Clump (spheres)		<p>PFC</p> <p>The clump is generated by using overlapped spheres with algorithm based on the 2D particle image. The particle volume, length and width can be obtained with the 2D image. Afterwards, based on them the positions of the spheres for the clump are confirmed.</p>	<p>Medium computation cost; medium shape reality; medium contact interlocking; three-dimensional with intermediately realistic performance (shear strength, repose angle). Using 2D image analysis method to build particle.</p>
13	McDowell [10]; Jing [39, 102]; Khatibi [36]; Kim [73]; Ferrellec [23, 103, 104]; Zeng [37]; Zhang [105]; Indraratna [20, 21, 58, 62]	Clump (spheres)		<p>PFC (Li, Jing, Khatibi, Ferrellec, Zeng, Zhang, Indraratna); Dynamic optimization method (Kim)</p> <p>The clump is generated by using overlapped spheres based on the 3D particle image. The method is explained in the Figure 1A.</p>	<p>High computation cost; high shape reality; high contact interlocking; three-dimensional with realistic performance (settlement, sleeper resistance, repose angle, shear strength). This method is used by many studies. The adjustable spheres per particle can satisfy the balance of the computation cost and the accuracy.</p>
14	Wang [106]; Zhou [107]	Clump (spheres)		<p>EDEM</p> <p>The clump is generated by using overlapped spheres with regular shapes. Two types of clumps are applied.</p>	<p>Medium computation cost; medium shape reality; medium contact interlocking; three-dimensional with intermediately realistic performance.</p>



15	Suhr [15, 19]; Miao [63]	Clump (spheres)		PFC (Liu, Miao); Yade (Suhr) The clump is generated by using spheres without overlaps into regular shapes. The clump is the same as No. 9, but it does not have sphere bonded as the asperity and also cannot break.	Medium computation cost; medium shape reality; medium contact interlocking; three-dimensional with intermediately realistic performance (shear strength).
16	Tutumluer, Huang [11, 18, 22, 29, 38, 42, 47, 49, 50, 55, 60, 74, 84, 108]; Saussine, Voivret [48, 67, 68, 70, 72, 109-111]; Elias [112]	Polyhedron		BLOKS3D (Tutumluer, Huang); LMGC90 (Saussine, Voivret); Yade (Elias) The generation method of the polyhedron is shown in Figure 1C.	High computation cost; high shape reality; high contact interlocking; three-dimensional with realistic performance (settlement, acceleration, shear strength, lateral resistance). Presence of the sharp corner and edge. But leading to great increase of computation cost due to contact detection and ambiguous contact force between edges.
17	Le Pen, Powrie [28, 33]	Potential particle		This type of spheropolyhedron is generated based on the real ballast particles. It starts from a sphere, afterwards, planes are used to cut the sphere, creating flat-spots on it. The plane orientations and locations planes can be control by the operator until the shape approaches the real ballast particle shape.	High computation cost; high shape reality; high contact interlocking; three-dimensional with realistic performance (shear strength). Lower computation cost than the polyhedron, but it cannot present concave particles.
18	Ji [43, 113]	Spheropolyhedron		The spheropolyhedron is generated using Minkowski sum theory together with the Voronoi diagram [43]. The Voronoi diagram is used to define random sizes and shapes for building the basic polyhedron. Afterwards, the vertices or edges of the basic polyhedron are replaced by spheres or cylinders respectively, using the Minkowski sum.	High computation cost; high shape reality; high contact interlocking; three-dimensional with realistic performance (Settlement). The sharpness of the edge and corner can be adjusted by changing the sphere/cylinder radius. This particle has lower computation cost than the polyhedron due to easier contact detection and contact force calculation.

196 The computation cost is ranked through ordering all the methods. For example, in the same test  
197 model, using the sphere (or disc in 2D) costs the lowest the time, while using the cluster takes the  
198 most time. Using the more complex cluster (with more spheres for one particle) takes more time.  
199 Particularly, it is considerably difficult to compare the computation cost between different types of  
200 basic elements (e.g. sphere or polyhedron). Because the parts that take main computation cost are  
201 different, specifically, the sphere element mainly spends the time on the force-displacement cycles,  
202 while the polyhedron element spends the time on the contact detection. In addition, until now the  
203 studies on the comparison of different DEM methods are relatively unexplored. Therefore, the  
204 relatively rough rank is given in the table according to other review papers in Ref. [88, 114, 115].

205 The realistic performance is decided based on comparing the results with results of the experimental  
206 tests and reality. For example, Lobo-Guerrero (Table 1; No. 1) used the discs to present ballast  
207 particles, the settlement is with very big errors. This is due to not only the discs are two-dimensional,  
208 but also the discs are prone to roll instead of translation motions. Even though sometimes the shear  
209 strength (Table 1; No. 2, 3) can be matched with the test results by using proper model parameters  
210 (e.g. friction, stiffness), however, in most cases the dilation results cannot be matched.

211 The shape reality is ranked based on how close the modelled particle is to the real ballast particle.  
212 For example, the simple sphere (or disc) has the lowest shape reality, and the clump (Table 1; No 13)  
213 has the highest shape reality when the sphere number for one particle is very large (over 1000). It  
214 needs to note that different basic elements are difficult to compare, therefore, the rank is more  
215 experiential instead of using very accurate calculations. Moreover, the rank is obtained according to  
216 other review paper [88, 114, 115], especially, in [88], the same rank means was applied.

217 The contact interlocking was proposed in the reference [24], which presented the performance  
218 comparison of simple sphere and the clump by simulating the ballast box test. The contact  
219 interlocking reflects how the particle movements are restricted. Ambiguous contact force between  
220 edges means the contact forces at the edge contacts are not clearly calculated.

### 221 2.1.2. Size

222 In practise, the particle size distribution (PSD) is widely utilised for particle size because of easy and  
223 rapid size results, which are based on sieving. Specifically, the PSD is a curve to present the  
224 percentages of each size range. Most of the DEM models utilise the PSD within the lower and upper  
225 bands of the grading specifications (standards [77-79]).

226 The particle size should be carefully calibrated in the DEM simulations, because the influences of the  
227 PSD on the performance (shear strength, settlement) [116] have not been confirmed. On one hand, it  
228 is logical that the particle size influences the assembly porosity, compaction and the total particle  
229 contact number, further influencing the performance. For instance, the performance of the  
230 wide/narrow PSDs are compared in [17, 108], which shows obviously different performance. On the  
231 other hands, some studies did not reach the same conclusion. For example, The study on this is  
232 introduced in [16], which utilises the direct shear test to study flaky and elongated ratio and the  
233 particle size distribution, show that the PSD has no clear relationships with the shear strength. This  
234 may be due to only using the PSD for particle size calibration is not sufficient to present the particle  
235 size. However, for now the PSD is the only way for presenting particle size, and the DEM particle size  
236 calibration method is to control both the DEM model PSD and the experimental test PSD within the  
237 same lower and upper bands.

238 To be more specific, in the DEM models, the PSD is calculated with the particle diameters when the  
239 spheres/discs are utilised as ballast particles, see [16, 65, 97, 117]. When the agglomerates (clumps,  
240 clusters or clump & cluster) are applied in the DEM models, the spheres/discs are initially generated  
241 in the model to archive the designated PSD, afterwards, the spheres/discs are replaced by the  
242 agglomerates with the various algorithms [9, 63]. When applying certain number kinds of  
243 agglomerate templates (with different particle sizes) to build a ballast sample, the designated PSD is  
244 achieved by setting certain percentages of each kind of template, e.g. [20, 24, 35, 36, 44, 61, 93, 99,

245 105, 118]. Likewise, the polyhedron (polygon) or spheropolyhedron also utilises this means to  
246 achieve the designated PSD [22, 33, 113]. It needs to note that limited studies use the same PSD of  
247 the tests to calibrate the particle sizes of a sample, see [31].

248 More importantly, the porosity (or bulk density) should also be calibrated, although the modelled  
249 PSDs are the same with the experimental PSDs. The porosity is calculated by the ratio of the void  
250 volume to the total volume. The total volume is generally counted as the volume of the test rig  
251 container. The bulk density is calculated by the ratio of the sample mass to the total volume. Due to  
252 the differences of the ballast material density can influence the bulk density results, the porosity is  
253 more suitable to describe the compaction degree of ballast assemblies.

### 254 2.1.3. Discussion

255 From the above descriptions for particle morphology (shape and size), the following five aspects  
256 might need discussion for improvement.

- 257 1. The DEM starts at using simple discs to present the ballast particles, afterwards the  
258 combinations of several discs (clump or cluster) are utilised for more accuracy. Another  
259 development is that the basic elements upgrade from 2D discs to 3D spheres. Both of these  
260 two developments lead to higher computational cost. Therefore, balancing the  
261 computational cost and the model accuracy is the main problem in current DEM models  
262 using the sphere/disc as the basic element.
- 263 2. Differently, the reason of high computational cost when using the other basic elements (e.g.  
264 polyhedron and potential particle) is the contact detection. In addition, current contact  
265 detection algorithms for non-sphere basic elements are not sufficiently logical [88].
- 266 3. The particle shape influences the particle interlocks and further the contact types and  
267 numbers. The contact types include the face-face contact, angle-face contact and edge-face  
268 contact etc. These contact types cannot be sufficiently presented in current DEM models.  
269 Particularly, the surface texture is only presented or adjusted by the friction coefficient, not  
270 only in model of the disc/sphere, but also of the polyhedron, spheropolyhedron or potential  
271 particles. More importantly, the face-face contact cannot be presented accurately, because  
272 using the sphere (or agglomerates) the contact area is too small, and the area is too large  
273 when using the other particles, e.g. polyhedron. Furthermore, the face-face contact is the  
274 main contribution to the contact forces in practise when the ballast assemblies are fully  
275 compacted.
- 276 4. The calibration of the particle shape is normally based on the macroscopic performance (e.g.  
277 shear strength). It is obvious that using particles as real as possible can perform more reliable  
278 simulation. However, this leads to larger computational cost, which is the largest problem.  
279 Therefore, considering some compensation at other aspects is a promising study direction.  
280 For example, the interlocks can also be presented by adding the rolling resistance at the  
281 contacts to restrict the relative disc/sphere rotations/movements. Using this method, the  
282 spheres or simple particles can also have the same performance [119], and this will be  
283 introduced in the Section Contact models.
- 284 5. Even though the particle size is considered when performing the DEM simulations through  
285 the PSD, none of the methods can present the real particle sizes. This is due to that the  
286 modelled PSD is not as precise as the real PSD, and more importantly, the real PSD is  
287 obtained from the sieving, which is not precise. Thus, the modelled PSD is not accurate to  
288 illustrate particle sizes. The polyhedron (polygon), spheropolyhedron or agglomerate is  
289 obtained based on the real particle, however, most studies only applied limited kinds of  
290 particle templates. In addition, after replacing the spheres/discs with agglomerates, the final  
291 PSD could be different from the designated one. Therefore, further studies should be  
292 performed at this direction to better calibrate the particle size.
- 293 6. For the porosity, it is easy to measure it in the DEM models, however, using the same  
294 porosity as in the experimental or field tests is very difficult. Because it is not easy to  
295 measure porosity accurately in practical situations, moreover, after a few cyclic loadings the

296 sample porosity has very big different changes. This phenomenon results from many reasons,  
297 such as, the ballast material and flaky and elongation ratio.

## 298 2.2. Ballast particle degradation

299 For railway ballast, until now, two main types of degradation are admitted, i.e., the breakage and the  
300 abrasion. However, no clear illustrations were found in the earlier studies, this definition is more  
301 experiential other than absolute. Nevertheless, the breakage generally presents the particle crush  
302 with new fracture surface. The abrasion is generally defined as fine-dropping due to wear with  
303 roughness reducing. Particle degradation is a possibly harmful phenomenon, which should be  
304 discreetly studied. This is due to 1) the particle degradation is the main reason to the ballast bed  
305 degradation and further more severely leading to the drainage problem and mud-pumping; 2) the  
306 particle degradation influences significantly on the ballast performance; 3) the particle degradation is  
307 the main reason to the track defects at some special area (e.g. transition zone).

308 Even though in earlier laboratory test studies, the factors influencing on the particle breakage are  
309 given, including the particle hardness, particle size, mineralogical composition, angularity, and  
310 compaction and particle grading [93]. However, almost all the references are from the studies on  
311 soils or sands, which have much smaller particle size than railway ballast [120-122]. Moreover, the  
312 particle breakage is only one aspect of the particle degradation, and the particle abrasion should also  
313 be considered.

314 Due to the significant influences of the ballast particle degradation, it should be carefully calibrated  
315 in the DEM models. Moreover, the factors influencing on the particle degradation should be  
316 considered during the calibration. In the following two sub-sections, how the breakage and abrasion  
317 are presented in the DEM models are introduced. Afterwards, the discussions on the aspects for  
318 improvement are given in the last sub-section.

### 319 2.2.1. Breakage method

320 Currently, the ballast particle breakage in the DEM models can be presented into two types, which  
321 are classified based on the basic elements. For the basic element of spheres/discs, two kinds of  
322 categories can be utilised to classify the breakage methods, i.e. the bonded-particle model (BPM) and  
323 the fragment replacement method (FRM) [123]. For the other basic elements, the only one study in  
324 [112] including particle breakage utilised the polyhedrons with the FRM as breakage method.

325 The BPM is to model a ballast particle as a cluster or clump & cluster. As described in Section 2.1.1,  
326 the cluster can break when the loading is large enough to break the bonds, which hold the spheres  
327 together. The FRM is to replace each original particle with several smaller particles that have almost  
328 the same area (for the 2D) or volume (for the 3D). In the polyhedron model [112], the original  
329 particle and the smaller particles (for replacement) have the same volume. The two breakage  
330 methods are shown in Figure 2.

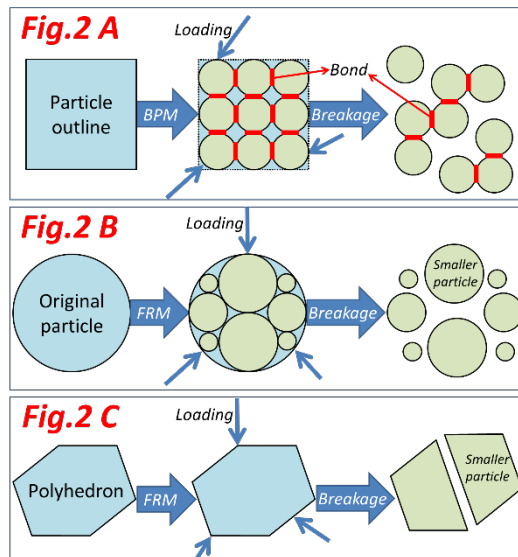


Figure 2 Illustration for ballast particle breakage methods [34, 46, 112, 121]

331  
332

333 The BPM has been utilised in most of the references, as shown in Table 2, while until now limited  
334 studies utilised the FRM. In Table 2, breakage method utilised in the references are presented with  
335 the BPM or the FRM. The breakage description column gives the breakage types with figures.

336 Two different types of the bond strength are utilised for the BPM in earlier studies, which can be  
337 described as 1) the parallel bond and 2) the contact bond strength. The two types of bond are two  
338 types of contact models (Section 2.3.1.2), and their corresponding parameters are given in Table 4.

339 The parallel bond gives the physical performance of a cement-like substance sticking together the  
340 two contacting particles [82]. When a force is acted on a parallel bonded particle, the particle  
341 develops a force and moment within the bond due to a relative motion between the corresponding  
342 two spheres. When the force applied on the particle exceeds the bond strength, the parallel bonds  
343 are removed together with the corresponding force and moment [82]. Five parameters are utilised  
344 for the parallel bond, namely shear and normal bond stiffness, normal and shear strength and  
345 parallel bond radius multiplier. From the reviewed studies, it can be seen that the shear and normal  
346 bond stiffnesses are set as a same value, and so are the shear and normal bond strengths.

347 The contact bond can be regarded that two contacted spheres are bonded by glue, and the constant  
348 normal and shear strengths are acted at the contact point. At the contact, the glue can provide  
349 normal and shear strengths. The contact bond prevents the relative motion (slip) by the shear force  
350 that is limited by the shear strength. When the acted shear force surpasses the shear strength, the  
351 bond fails. But the contact forces are not changed, which are provided by the product of the friction  
352 coefficient and normal force (shear force), and by the compressive normal force (normal force).  
353 When the acted normal force is over the normal strength, the contact bond fails, and both the  
354 normal and shear forces are set to zero [82]. Two parameters are utilised, i.e. the shear and normal  
355 strengths.

356 The other columns in Table 2 present the calibration methods include the bond strength, inner  
357 particle number/size in clusters, particle type, applied laboratory test and breakage criterion. For the  
358 BPM, the contents are mainly about the calibration methods that help to present the breakage more  
359 realistic. For the FRM, the breakage criterion is given as well as the calibration methods. The  
360 breakage criterion triggers the particle replacement by unbonded smaller particles and should be  
361 pre-defined, as shown in the last column (Table 2).

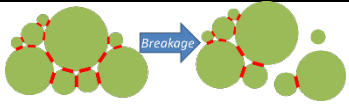
362 Regarding the inner particle number/size, an example from [95] (Table 2 ;No. 3) is given for  
363 explanation. The spheres are bonded to model one crushable particle. Afterwards, some of the  
364 spheres are removed randomly for reducing the particle strength, thus the distribution of the

365 strengths can follow the Weibull distribution. It also demonstrates that the sphere size has effects on  
366 the average strength.

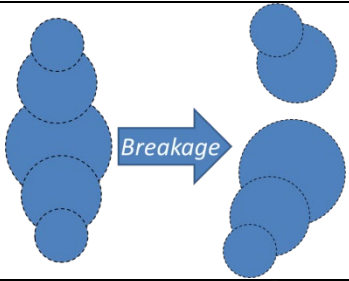
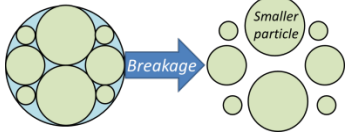
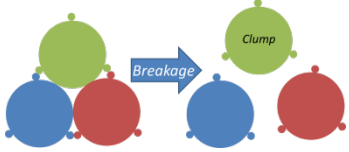
367 The particle type means that if the component spheres/discs have overlaps, and this is only for the  
368 BPM. The modelled laboratory tests are the tests that are utilised for producing the particle breakage,  
369 such as the single particle crush test, including the triaxial test (biaxial test in 2D), sleeper-ballast  
370 track model, single particle crush test, ballast box test and direct shear test. It needs to note that the  
371 large-scale oedometric test (Table 2; No. 7) is similar to the cyclic triaxial test.

372 Finally, the summary column is given in Table 2. It describes the advantages and disadvantages of this  
373 method, and more importantly its innovation together with developments. In addition, the breakage  
374 criterion for each FRM is given.

375 Table 2 Particle degradation in the DEM model calibration (figures reproduced from the given references)

No.	Reference	Breakage description	Breakage method	Bond parameter	Inner particle	Particle type	Modelled laboratory test	Breakage criterion/Advantage-disadvantage
1	Indraratna [34, 44]; Xiao [31]; Mahmoud [45]		BPM	Parallel bond: Stiffness, 6e10 N/m <sup>3</sup> ; strength 5e6 N/m <sup>2</sup> ; radius, 0.5 [31, 34] <hr/> Parallel bond: Stiffness, 6.25e10 N/m <sup>3</sup> ; strength, 5.78e6 N/m <sup>2</sup> ; radius, 0.5 [44] <hr/> Contact bond: 9.42e3 kN [45]	Different size discs	No overlaps	Cyclic biaxial test [34]; large-scale track process simulation test [44]; 3-sleeper track model [45]	1. Save computation time by presenting crushable particles with less discs (due to different size discs). 2. However, the breakage type is dependent on the parallel bond breakage, and the parameters for the parallel bond are not clearly defined or well-calibrated (lack of verification). 3. But this can lead to random breakage types, and in practise the random is similar to the reality.
2	Mahmoud [45]	Diagram shown in Figure 2A	BPM	Contact bond: 9.42e3 kN	Same size discs	No overlaps	3-sleeper track model	1. Higher computation cost due to the same size discs (larger amounts of discs) are used in one particle. 2. However, breakage type is more diverse than the particle with the different size discs, and the parameters for the parallel bond are not clearly or well-calibrated (lack of verification). 3. Additionally, the same size discs lead to more parallel bonds between them, adjusting the parallel bond number is also not confirmed (lack of verification).
3	McDowell [95]; Qian [53]; Liu [65]	Diagram shown in Figure 2A (but in 3D)	BPM	Contact bond: 2.1e3 kN [95] <hr/> Parallel bond: Stiffness, 3e14 N/m <sup>3</sup> ; strength, 3e8 N/m <sup>2</sup> ; radius, 0.5 [53] <hr/> Parallel bond: Stiffness, 1.8e5 N/m <sup>3</sup> ; strength, 6e10 N/m <sup>2</sup> ; radius, 1.0 [65]	Same size spheres	No overlaps	Single particle crush test, ballast box test [95]; Single particle crush test [53]; Triaxial test [65]	1. Highest computation cost due to large amounts of spheres (3D) and parallel bonds. 2. Another issue is larger numbers of parallel bonds need be reduced and proper strength/stiffness value should be chosen for the parallel bond. Because the particle can break (one part released) only when the corresponding parallel bonds are broken. 3. When the component spheres are small enough for one particle, the real degradation process (e.g. wear, flaking) can also be presented.



4	Dahal [41]		BPM	Parallel bond: Stiffness, 6e10 N/m <sup>3</sup> ; strength, 3e7 N/m <sup>2</sup> ; radius, 0.5	Different size spheres	Overlaps	2-sleeper half-track model	1. Save computation time by presenting crushable particle with less spheres (due to the overlapped different size spheres). 2. The overlapped spheres can present better particle shape (surface roughness) and provide higher interlock between particles. 3. However, after breakage, the total volume increases, which is not realistic. 4. It needs to note that the parallel bond parameters have the same problem as the above introductions.
5	Lobo-Guerrero [46, 89, 90, 124]		FRM	-	Different size discs	No overlaps	Uniaxial compression test; Direct shear test	Particles that have coordination number equal to or smaller than 3 can break if the induced tensile stress $\sigma_t$ is larger than the tolerable maximum stress $\sigma_{max}(r)$ , which is calculated with the following equation: $\sigma_{max}(r) = \sigma_{max1mm}(r)^{-1}$ . In the equation, the $\sigma_{max1mm}$ is $3 \times 10^6$ Pa and $r$ is the particle radius.
6	Alaei [93]		FRM	-	Different size discs	No overlaps	Single particle crush test; Biaxial test	The particle can break when meet the criterions that are related with two aspects, confinement (contact force orientation anisotropy) and maximum tensile stress. The contact force orientation anisotropy ( $A_f$ ) exceeds 0.33, and the induced tensile stress $\sigma(r)$ is over $\sigma_{max}(r)$ . The $A_f$ is expressed as follows: $A_f = (f_\theta)_{max} / \sum f_\theta$ . In the equation, $f_\theta$ is the absolute value sum of the forces (applied on this clump) that are oriented at the direction between $\theta$ and $\theta+20$ . The $\sigma_{max}(r)$ is expressed as follows: $\sigma_{max}(r) = 1.4d^{\lambda-2}$ . In the equation, $\lambda$ is a material parameter and has a specific value for specific rock material; $d$ is average dimension of the clump.
7	Elias [112]	Diagram shown in Figure 2C	FRM	-	Polyhedron	-	Large-scale oedometric test	The particle can break when the splitting stress ( $\sigma_e$ ) exceeds the particle strength ( $f_t$ ). The splitting stress ( $\sigma_e$ ) is expressed as follows: $\sigma_e = \sqrt{[(\sigma_1 - \sigma_2)^2 + (\sigma_1 - \sigma_3)^2 + (\sigma_2 - \sigma_3)^2] / 2}$ . In the equation, $\sigma$ is obtained with the equation: $\sigma = \sum_c l_i^{(c)} F_j^{(c)} / V$ . In the equation, $F^{(c)}$ is the force applied at the contact point (c) and the contact position is $l^{(c)}$ ; $V$ is the particle volume. The particle strength ( $f_t$ ) is expressed as: $f_t = f_0 \sqrt[3]{4\pi / (3V)}$ . $f_0$ is dependent on the material (MPa); $V$ is the particle volume.

376 Note: 6e10 is scientific notation, it is 60,000,000,000

377

378 2.2.2. Abrasion presentation method

379 The ballast particle abrasion is another type of ballast particle degradation. In the DEM simulations, it  
380 can be generally presented by two means, which is dependent on the applied basic elements (Figure  
381 3). One applies the basic elements of sphere (disc in 2D), and releasing the small sphere(s) at the  
382 asperity is the mean to present abrasion [25, 54, 80]. For the basic elements of sphere (disc in 2D),  
383 two methods of small particle release can be utilised, 1) releasing by replacement and 2) releasing by  
384 breaking the parallel bond, as shown in Figure 3 A/B. The other applies the potential particle, and  
385 replacing the asperity a more rounded cap is the applied means (Figure 3C) [28], and this is  
386 developed based on a new contact model, conical damage model (introduced in Section 2.3.2). The  
387 potential particle introduction can be found in Table 1 (No. 17).

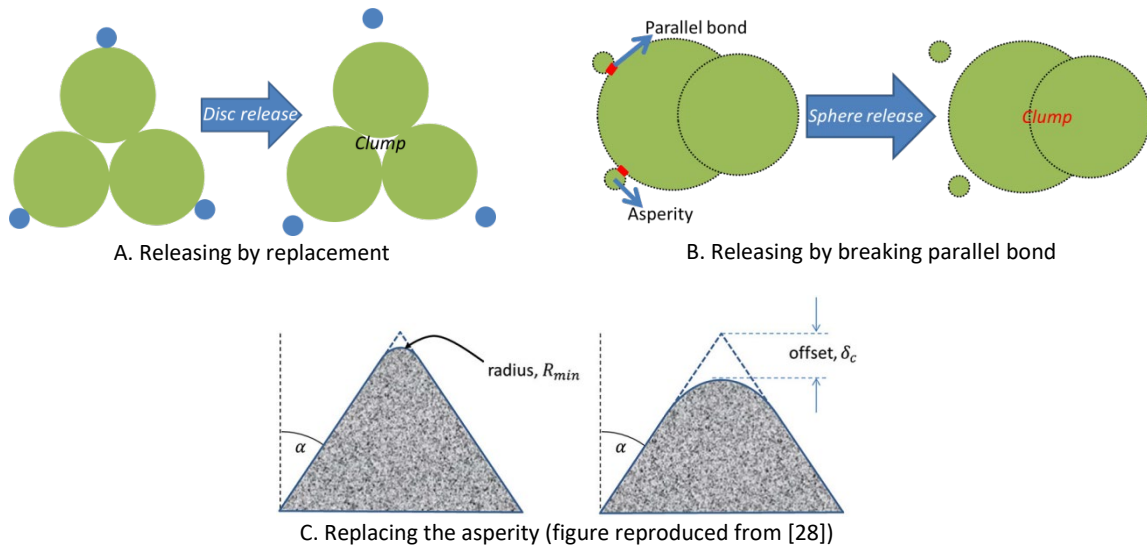


Figure 3 Two general means for presenting abrasion

388

389 2.2.2.1. Sphere/disc

390 To be more specific, the abrasion presentation method in [54] is the type that is shown in Figure 3A.  
391 The method is based on the FRM, and different size discs are utilised in one particle. In their study,  
392 the biaxial test is simulated. During the tests, a small disc is released from main body once the  
393 induced stress that acts on the particle is larger than 10 MPa, additionally, the particle must have the  
394 coordination number on more than three. From the above information, it can be seen that the  
395 disadvantage of this method is how ballast particle is worn is fixed.

396 The disadvantage can be partly solved in the studies [25, 80]. They applied the BPM (breakage  
397 method) by bonding small spheres with the main body (clump) as shown in Figure 3B. The small  
398 spheres can be released when the applied force exceeds the parallel bond strength. This means the  
399 abrasion can be more accurately simulated by releasing the spheres at the correct position that the  
400 force is acted on. The basic element is sphere (in different sizes) in the two studies, which is another  
401 improvement.

402 It needs to note that in [53, 65, 95] the ballast abrasion can also be presented when the sphere/disc  
403 is small enough to present the sharp corner (Figure 2A). However, presenting sharp corner with this  
404 method costs large amount of computational time.

405 2.2.2.2. Potential particle

406 As shown in Figure 3C, the abrasion presentation method in [28] is to replace the asperity tip with a  
407 more rounded cap, when the applied stress exceeds the affordable material strength. In the study,  
408 the triaxial test is simulated. Until now, only this study applied the abrasion process in the DEM  
409 models in railway ballast studies that utilise the polygonal particles. Two main concerns can be seen.  
410 On one hand, the abrasion criterion is difficult to calibrate. On the other hand, the abrasion process  
411 produces small particles in reality, which have not been presented.

### 412 2.2.3. Discussion

413 From the introduction and summary (Table 2), the following aspects about ballast particle  
414 degradation calibration in DEM models can be observed. Two types of breakage presentation  
415 method (BPM, FRM) are mostly applied for the DEM breakage calibration. For the abrasion  
416 presentation, limited studies have been performed, and only one study was found using the  
417 polygonal particles, potential particles, instead of sphere-based particles. The methods of ballast  
418 breakage calibration are relatively numerous, however, the methods for presenting the abrasion are  
419 not a lot, especially for the roughness reduction. For abrasion, until now, only the angularity (sharp  
420 corner) loss can be presented. The improvement aspect is obvious that is after breakage in practise  
421 the fresh fracture face can provide higher resistance force, however, in the DEM this has not been  
422 developed or presented. Therefore, capturing the two kinds of degradation phenomenon still needs  
423 some further studies. For calibrating the breakage of the basic element sphere (or disc), the bond  
424 strength is generally changed to match the results of the single particle crush test [122]. For abrasion,  
425 until now, two methods are used. One is using the bond breakage to present sharp corner loss and  
426 the calibration is dependent on the bond strength, however, the reason for using the bond strength  
427 value is not clearly given until now. No tests were found until now to calibrate the bond value for  
428 abrasion.

429 For the BPM, the insufficiencies are mainly related with two aspects. On one hand, large model  
430 cannot be built due to the computational cost is high. On the other hand, the parameters of the bond  
431 between spheres/discs are difficult to confirm with current studies. Specifically, the following  
432 discussions are given:

- 433 1. The BPM is more suitable for single particle crush study or similar small-scale model, due to  
434 the computational cost is very high when applying the BPM for degradation calibration.  
435 Because not only every spheres/discs in the cluster need to take calculation time (contact,  
436 force and displacement detection), but also the additional time spent on calculating the  
437 equations for bonds (parallel bond or contact bond). The equation for bonds means that the  
438 relative motions and forces between spheres within a cluster (discs in 2D) should be  
439 calculated every cycles.
- 440 2. In addition, the parameters for the bond (parallel or contact bond) need further studies on  
441 calibration and validation to present more realistic ballast breakage. Specifically, two main  
442 parameters, the bond numbers and bond stiffness, are not confirmed. For example, on one  
443 hand, the parameters of the shear and normal bond stiffness (or strength) are to use the  
444 same value until now. On the other hand, the proper and optimal bond numbers and  
445 stiffness are not confirmed, and more importantly, they are strongly related with the  
446 computational cost.
- 447 3. The BPM cannot provide further particle breakage, when the fractures of the particle have  
448 crushed into one single sphere (disc in 2D) not the assembly of the bonded spheres. This  
449 means one single sphere cannot further crush after it is released from the main particle,  
450 because the breakage is presented by breaking the bonds between spheres and only one  
451 sphere alone does not have the bonds.
- 452 4. To date, for the railway ballast studies, the single particle crush test is the only test applied  
453 for breakage validation. It still remains big challenges in this direction. Specifically, it is to fit  
454 the fractal dimensions of the single particle crush test results with the Weibull distribution.  
455 However, in reality, the breakage is dependent on plenty of factors, e.g. the ballast material,  
456 surface micro-crack, inner crack, particle shape and acting point of force. Therefore, specific  
457 DEM model parameters for specific situation is of great importance for the model calibration.
- 458 5. Because the contact between two spheres of one ballast particles remain after the contact  
459 bond (defined in Section 2.2.1) breaks. The contact can still provide the normal and shear  
460 stiffness that may be the same as that the contact bond provides. This means that after the  
461 contact bond breaks, it might not change the performance of the ballast assemblies as much  
462 as realistic breakage.

463 6. The parallel bond can solve the above-mentioned issue. This is due to the parallel bond  
464 stiffness and contact stiffness are combined, which means the performance of the stiffness is  
465 the sum of the two kinds of stiffness. The parallel bond breakage immediately induces that  
466 only the contact stiffness remains, which leads to the performance reduction of ballast  
467 assemblies as reality. Nevertheless, the parallel bond breakage induces the moment  
468 elimination, and this means the restricted rotation (by parallel bond) between two spheres  
469 (or two parts) is released. This lowers the simulated results of unconfined compressive  
470 strength.

471 For the FRM, the improvements can be made at the two aspects, i.e. breakage criteria and fracture  
472 replacement. The breakage criteria are the self-developed algorithms that describe the conditions for  
473 breakage. Once the conditions are reached, the particle is replaced by fractures. The improvement  
474 for fracture replacement is to confirm the most suitable and realistic fracture means. Based on these  
475 two aspects, the following discussions are given:

476 7. It is difficult to confirm if the current breakage criterions are realistic and accurate, especially  
477 for further studies on performance changes induced by particle breakage.

- 478 • Firstly, in reality, the breakage is mostly dependent on the natural properties, e.g.  
479 the parent rock material (strength), ballast shape (non-cubic) and inner/surface  
480 cracks. These are much more difficult to control or predict than laboratory test  
481 conditions. However, until now, most of the breakage criterions are based on the  
482 study in [46], which utilised the laboratory test condition (low confining pressure;  
483 coordination number  $\leq 3$ ) for making the breakage criterion. The breakage criterion  
484 can be more realistic and reliable once the ballast physical properties are considered.
- 485 • Secondly, the breakage criterions for different particle morphology (shape, size)  
486 should be different, however, this has not been successfully developed until now.  
487 Particle morphology is very important when studying the particle breakage. Because  
488 the non-cubic (flaky or elongated) particles are more prone to break than the cubic  
489 particles [125].
- 490 • Finally, to date few studies applied 3D ballast particles for the FRM, and the breakage  
491 criterion in 3D is more complex than in 2D. For this, the breakage criterion for 3D  
492 model is necessary to develop. For example, the contacts between particles of 3D  
493 models are more than 2D models, which means the criterion of coordination number  
494  $\leq 3$  cannot be directly used in 3D models. In addition, the particle displacements of  
495 the 3D models are more diverse than the 2D models, which leads to the bigger  
496 compaction and porosity differences and further causing inner stress differences of  
497 ballast assemblies.

498 8. The fracture replacement usually needs to meet three requirements: 1) The fracture sizes  
499 and number should be as less as possible to keep the computational efficiency; 2) it is  
500 necessary to confirm the correct and suitable fracture sizes and number (Figure 2B) that can  
501 present the accurate and realistic performance change of ballast assemblies with particle  
502 breakage (e.g. sharp stress reduction); the fracture sizes and number should obey the mass  
503 conservation compared with the original particle.

- 504 • Computational efficiency: The FRM can increase the total sphere/disc numbers once  
505 breakage occurs, which can considerably increase the computational cost, because in  
506 the DEM the sphere/disc number and the contact number decide the computational  
507 cost each calculation cycle. It means the fracture sizes and number decide to what  
508 extent the simulation can last and how many times the particle can break.
- 509 • Correct and suitable fracture sizes and number: Earlier studies decide the fracture  
510 sizes and number by the single particle crush test. However, the fracture sizes and  
511 number are related considerably with the particle physical properties in reality, e.g.  
512 material, particle size and shape and inner/surface crack. Therefore, it is necessary to  
513 obtain the correct and suitable fracture sizes and number based on the real breakage

514 in reality, especially, when the above-mentioned physical properties are considered.  
515 This can significantly improve the model accuracy.  
516 More importantly, the performance of ballast assemblies is dependent on the  
517 fracture sizes and number. Because the fracture sizes and number can change the  
518 particle size distribution (or grading), further influencing the consolidation of the  
519 ballast assemblies. The consolidation decides the ballast performance and the  
520 further step ballast bed degradation. Moreover, the short term performance (e.g.  
521 sharp stress reduction) also needs correct fracture sizes and number to present.  
522 It needs to note that it is relatively undeveloped that how to produce correct  
523 fracture sizes and number based on the contact forces between the particles. A  
524 particle in the ballast assemblies has contacts at different directions (more complex  
525 in 3D model), and different contacts for one particle could lead to different breakage.  
526 Particularly, different breakage due to diverse conditions (e.g. contact force  
527 difference) can be presented by using not only sphere with different sizes but also  
528 clumps. In addition, the demand of model in 3D is also necessary at the aspect of the  
529 fracture replacement.

- 530 • Mass conservation: From the earlier studies, it can be observed that the fractures  
531 cannot fully fill the original sphere (Figure 2B). This leads to the mass conservation  
532 problem, which means the mass is smaller after replacing the sphere with fractures.  
533 Towards this, compensation methods should be proposed. Two possible methods  
534 could be useful, i.e. expansion method and density-change method. The expansion  
535 method is to expand the fracture (increasing the sub-sphere volume) to reach the  
536 original sphere volume. The density-change method is to increase the fracture  
537 density to reach the original sphere mass.

### 538 2.3. Contact models

539 The overall constitutive performance of the railway ballast assemblies in DEM is to a large extent  
540 decided by the applied contact model between each two ballast particles. In practise, the contacts  
541 between ballast particles are a complicated and highly non-linear issue. However, in the DEM models,  
542 the contact is simplified and the interaction is presented by using the constitutive contact models. A  
543 few parameters are defined that are related with the basic element (sphere/non-sphere), particle  
544 velocity, radius and material properties. Moreover, for the consideration of the energy dissipation,  
545 parameters for damping are also necessary to define.

546 In the Table 3-Table 5, the applied contact model and the corresponding parameters are given. In the  
547 following sub-sections, the contents in the table are explained, e.g. how each contact model works.  
548 Summarising them could provide the researchers a better view of the contact model differences,  
549 which can help better contact model selection and further develop new contact models.

#### 550 2.3.1. Basic element sphere/disc

551 For the sphere as basic element, the PFC is the most widely-used one with sphere/disc as basic  
552 element. The contact models applied in railway ballast studies can be classified into two parts: 1)  
553 models for particle interaction; 2) models for particle creation.

##### 554 2.3.1.1. Models for particle interaction

555 The following contact models are mostly utilised for the interaction between ballast particles in DEM  
556 model, including the linear model, Hertz contact model, rolling resistance model and conical damage  
557 model. The linear model is the most widely-used one, and the Hertz contact model (HCM) comes  
558 after. It needs to note that the rolling resistance model and the conical damage model are recently  
559 developed and have great potential for further application in railway ballast simulation. The detailed  
560 information (reference, software, parameters) is given in Table 3.

561 **Linear contact model:** The linear contact model (LCM) is the first contact model (simplest) applied in  
562 [12], and specifically it applies the linear and dashpot components (an elastic stiffness device and a

563 damper) for energy transfer and dissipation at both normal and tangential directions. The no-tension  
 564 linear elastic stiffness and the friction are provided by the linear component, and the viscosity is  
 565 provided by the dashpot component. The two components act through a very small area (the contact  
 566 point), and consequently only transfer forces (no contact moment). The addition of the linear  
 567 component ( $F_l$ ) and the dashpot component ( $F_d$ ) makes the contact force ( $F_c$ ;  $F_c = F_d + F_l$ ), as shown  
 568 in Figure 4A.

569 For the ballast material, no viscos behaviour exists at the contacts between ballast particles.  
 570 Therefore, the dashpot component in most cases is inactive, particularly, it is not described or  
 571 mentioned in most of the ballast studies using the PFC, e.g. in Ref. [17, 24, 62].

572 The linear component is the combination of normal and shear forces ( $F_l^n$ ;  $F_l^s$ ), and they can be  
 573 expressed as shown in Equation 1 [115]. In the equation, the  $k_n$  and  $k_s$  are the normal and shear  
 574 stiffness, respectively. The  $\delta_n$  and  $\Delta\delta_s$  are the contact overlap at normal direction and the tangential  
 575 overlap increment, respectively. The  $(F_l^s)_0$  is the previous timestep shear force. The  $\mu$  is the friction  
 576 coefficient.

577 Equation 1 (a)  $F_l^n = k_n \delta_n$   
 578 (b)  $F_{l*}^s = (F_l^s)_0 + k_s \Delta\delta_s$   
 579 (c)  $F_l^s = \begin{cases} F_{l*}^s & \text{if } F_{l*}^s \leq \mu F_l^n \\ \mu F_l^n & \text{if } F_{l*}^s > \mu F_l^n \end{cases}$

580 It needs to note that in most of the DEM models (using the PFC) with the linear contact model, the  
 581 particle kinetic energy is dissipated by the frictional sliding and the local damping with the default  
 582 value 0.7. The local damping is counted as particle attribute (not contact model parameter) in the  
 583 PFC, and it applies a damping force to each particle. For example, when the local damping takes the  
 584 default value 0.7, it dissipates the 70% of the unbalance force every timestep. The local damping is  
 585 more suitably applied for static or quasi-static simulations (e.g. single sleeper push test [36]) than the  
 586 dynamic simulation (e.g. large-scale process simulation test [32]). Because only using the local  
 587 damping is not enough to dissipate the accumulated energy when cyclic loadings are applied. More  
 588 severely, when the loadings are mostly rapid or high frequency impacts (e.g. tamping process) [81].

589 [Hertz contact model](#): The Hertz contact model (HCM) considers non-linear solution for the forces and  
 590 corresponding displacements. It approximately comes from the theory of Mindlin and Deresiewicz  
 591 theory [126]. For both the normal and tangential force-displacement, the smooth elastic sphere  
 592 deformation is theoretically analysed at the frictional contact.

593 The shear modulus is utilised for the shear force, and it is also dependent on the normal force. The  
 594 contact allows the happen of relative rotation, which means the moment is zero ( $M_c \equiv 0$ ). The contact  
 595 force ( $F_c$ ) is resolved into a Hertz component ( $F_h$ ) and dashpot component ( $F_d$ ).

596 Equation 2

(a)  $F_c = F_h + F_d$

(b)  $F_h^n = k_n \delta_n^{3/2}$

(c)  $F_h^s = (F_l^s)_0 + k_s \Delta\delta_s$

(d)  $k_n = \frac{4}{3} E^* \sqrt{R^*}$

(e)  $k_s = 8 G^* \sqrt{R^* \delta_n}$

(f)  $R^* = \frac{R^i R^j}{R^i + R^j}$

(g)  $E^* = \left( \frac{1-v_i^2}{E_i} + \frac{1-v_j^2}{E_j} \right)^{-1}$

(h)  $G^* = \left( \frac{2-v_i}{G_i} + \frac{2-v_j}{G_j} \right)^{-1}$

597 Because the ballast material is not viscos, therefore, the dashpot component is inactive in the earlier  
 598 studies [10, 99] in Table 3. The local damping is applied (introduced in the Linear contact model),  
 599 which is the same as the linear contact model.



600 The Hertz component is further calculated by the combination of normal and shear forces ( $F_h^n, F_h^s$ ).  
 601 They are expressed in the Equation 2 (b/c), respectively. In the Equation 2,  $G$  is the shear modulus;  $E$   
 602 is the Young's modulus;  $\nu$  is the Poisson's ratio;  $R$  is the particle radius;  $\delta_n$  and  $\Delta\delta_s$  are the contact  
 603 overlap at normal direction and the tangential overlap increment, respectively. It needs to note that  
 604 the equations of the Hertz contact model are given in [115], which are slightly different from the  
 605 equations in the commercial software, i.e. the PFC and the YADE. In the software, only one type of  
 606 modulus (shear or Young's modulus) is needed, because the quantified relationship between shear  
 607 modulus and Young's modulus can be obtained due to the particle isotropy.

608 **Rolling resistance linear model:** The rolling resistance linear model (RRLM) is based on the LCM,  
 609 specifically, a rolling resistance algorithm is added to the LCM. The RRLM applies a turning moment  
 610 to the contact area to counteract relative rotation. In the RRLM of the PFC, one extra parameter is  
 611 introduced (i.e. rolling friction) compared with the LC model. To be more specific, the difference  
 612 between the two contact models is the rolling friction, which is able to resist the particle rotation.  
 613 Particularly, the maximum value of restriction equals to the product of the rolling friction with the  
 614 corresponding normal force. The restriction effect can be regard as the rolling stiffness, which is  
 615 similar to the clockwork spring (Figure 4C). It needs to note that only the relative bending is resisted  
 616 by the RRLM at contact areas.

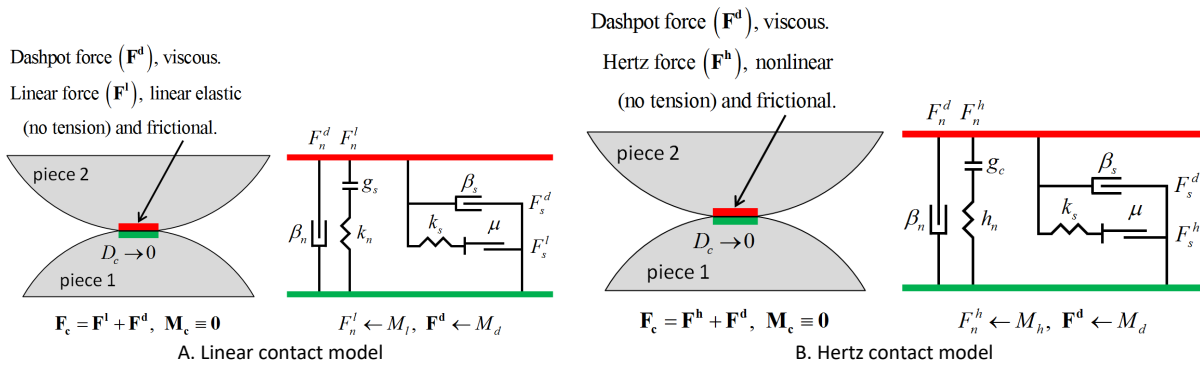
617 The contact force is calculated with the same means given in the Linear contact model. The rolling  
 618 resistance moment ( $M_r$ ) is calculated by the following equations. In the equations,  $M_r^0$  is the previous  
 619 timestep resistance moment;  $\Delta\theta_b$  is the relative bend-rotation increment;  $K_s$  is the shear stiffness;  $R^*$   
 620 is the effective radius in Equation 2(f);  $\mu_r$  is the rolling friction;  $F_t^n$  is the normal linear contact force.

621 Equation 3 
$$M_r = \begin{cases} M_r^0 - k_r \Delta\theta_b, & \|M_r\| \leq M^* \\ M^* (M_r / \|M_r\|), & \text{otherwise} \end{cases}$$

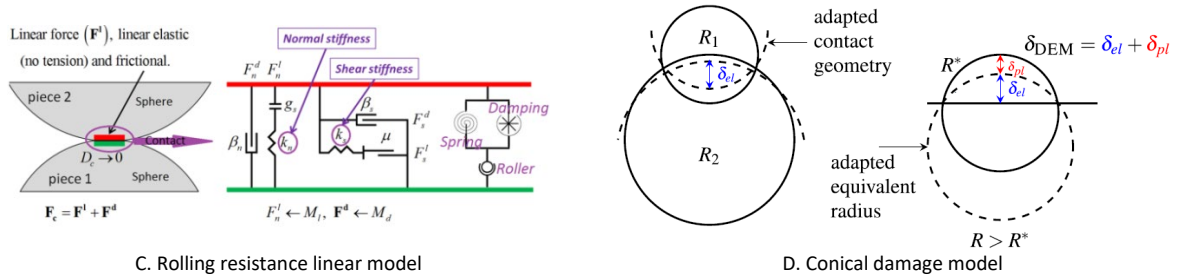
622 
$$k_r = k_s (R^*)^2$$

623 
$$M^* = \mu_r R^* F_t^n$$

624 For railway ballast, the studies using the RRLM defined diverse parameters due to they applied  
 625 different software. In PFC, the rolling friction is utilised. However, in [14] the authors applied the  
 626 open source DEM software (DEMPack) with different parameters from the PFC. Specifically, the shear  
 627 modulus and Poisson's ratio are utilised instead of the normal and shear stiffness, and another  
 628 parameter is the restitution coefficient. The restitution coefficient is the same function as the local  
 629 damping, but with different definition. For example, when the local damping is 1.0, it means the  
 630 particle would not move after applied a force. By contrast, if the restitution coefficient is 1.0, it  
 631 means the particle would move according to the applied force without any deduction.







C. Rolling resistance linear model

D. Conical damage model

Figure 4 Contact models for particle interaction(reproduced from [19, 82])

632

633 **Conical damage model:** The conical damage model (CDM) was first proposed in [28] and used  
 634 between the potential particles (introduced in Section 2.3.2). A more accurate and non-iterative  
 635 solution was proposed in [19] and used between particles (sphere-based), which applied different  
 636 formulation and more efficient algorithm. In the CDM, the classical Hertz–Mindlin model is applied to  
 637 the model material behaviour for the elastic part of the overlap ( $\delta_{el}$ , Figure 4D). When the stress  
 638 increases over the threshold, the contact area (expressed as  $R$  increment) increases along with the  
 639 plastic part of the overlap ( $\delta_{pl}$ ) appearing, which can be treated as damage occurs (Figure 4D). A  
 640 more tribological tangential contact law is applied for the shear force. It calculates the friction  
 641 coefficient value according to the normal stress, and during the calculation the contact area  
 642 increment is also valid.

**Algorithm for normal contact (conical damage model)**

Input parameters:  $E^*$ ,  $\beta$ ,  $\sigma_{max}$   
 Initial value assignment:  $\delta_{pl} = 0$ ;  $R = R^*$   
 Function ( $\delta_{DEM}$ ;  $R$ ;  $\delta_{pl}$ ):  
 $\delta_{el} = \delta_{DEM} - \delta_{pl}$   
 if  $\delta_{el} < 0$  then  
 $F_n = 0$   
 return  $F_n$   
 end if  
 $\sigma_0 = \frac{2E^*}{\pi} \sqrt{\frac{\delta_{el}}{R}}$   
 if  $\sigma_0 > \sigma_{max}$  then  
 $R = \frac{\delta_{DEM} + R^* \beta}{\left(\frac{\pi \sigma_{max}}{2E^*}\right)^2 + \beta}$   
 $\delta_{pl} = (R - R^*) \beta$   
 $\delta_{el} = \delta_{DEM} - \delta_{pl}$   
 end if  
 $F_n = \frac{4}{3} E^* \sqrt{R} (\delta_{el})^{3/2}$   
 return  $F_n$   
 End function

A. Algorithm for the normal force calculation

$$F_s = \begin{cases} F_s & \text{if } F_s \leq \mu F_n \\ \mu F_n & \text{otherwise} \end{cases} \quad F_s = F_s^{(0)} + 8G^* \sqrt{R \delta_{el}} \Delta \delta_s$$

$$\mu(\sigma_m) = \mu_0 + \frac{c_1}{1 + c_2 \sigma_m} \rightarrow \sigma_m = \frac{F_n}{R \delta_{el} \pi}$$

$$\mu_0 + c_1 \leq \mu(\sigma_m) \leq \mu_0 + \frac{c_1}{1 + c_2 \frac{2}{3} \sigma_{max}}$$

B. Equations for the shear force calculation

643

Figure 5 Explanation for the normal and shear force calculation method of the CDM [19]

644 The algorithm (equations) of the normal force calculation is given as shown in Figure 5A. In the  
 645 algorithm,  $E^*$  is the Young's modulus;  $\beta$  is a material parameter that can be expressed as  $\beta =$   
 646  $1 - \sin(\alpha)/\sin(\alpha)$ , and  $\alpha$  is the opening angle of conical asperity;  $\sigma_{max}$  is maximum stress for elastic  
 647 overlap;  $R$  is the contact area radius;  $R^*$  is the equivalent radius;  $\delta_{DEM}$  is the overall overlap.

648 The shear force is calculated based on the modified no-slip Mindlin law (Figure 5B), particularly, the  
 649 described radius-increasing method is also applied during the calculation. Another development is  
 650 the friction coefficient is not a constant value and it changes according to the normal force ( $F_n$ ),  
 651 contact area radius ( $R$ ) and the elastic part of the overlap ( $\delta_{el}$ ). In the equation, the  $\mu_0$ ,  $c_1$  and  $c_2$  (unit,  
 652  $\text{Pa}^{-1}$ ) are model parameters.

Contact model	Reference	Software; Particle type	Normal stiffness; Shear stiffness (N/m)	Friction coefficient	Normal damping ratio; Shear damping ratio	Damping
LCM	Zhang [8]	PFC; 2D; Clump	2.5e8; 2.0e8	0.5	0.01; 0.01	Not mentioned
LCM	Zhang [105]	PFC; 3D; Clump	1.5e7; 1e7	0.5	0.15; 0.15	Not mentioned
LCM	Jing [9, 39]	PFC; 3D; Clump	1.5e9; 0.77e8	0.8	Not mentioned	Not mentioned
LCM	Jing [17]	PFC; 3D; Clump	5e8; 5e8	0.5	Not mentioned	0.7
LCM	Jing [102]	PFC; 3D; Clump	1e8; 1e8	0.5/0.47	Not mentioned	0.7
LCM	Mishra [16]	PFC; 3D; Clump	5e5; 5e5	0.4	Not mentioned	0.7
LCM	Indraratna [20, 21, 61, 62]; Miao [63]	PFC; 3D; Clump	5.2e7; 5.2e7	0.8	Not mentioned	Not mentioned
LCM	Indraratna [44]	PFC; 2D; Cluster	3.58e8; 3.58e8	0.8	Not mentioned	Not mentioned
LCM	Indraratna [54]	PFC; 2D; Clump	5e9; 2.5e9	0.5	Not mentioned	Not mentioned
LCM	McDowell [23, 25, 26, 32, 57]	PFC; 3D; Clump	6e5/1e8; 6e5/1e8	0.6/0.8	Not mentioned	Not mentioned
LCM	McDowell [103]	PFC; 3D; Clump	1e7; 1e7	0.7	Not mentioned	Not mentioned
LCM	McDowell [104]	PFC; 3D; Clump	6e7; 6e7	0.6	Not mentioned	Not mentioned
LCM	McDowell [24]	PFC; 3D; Clump	5.08e9; 5.08e9	0.5	Not mentioned	Not mentioned
LCM	McDowell [27, 80]	PFC; 3D; Clump	1e9; 1e9	0.5	Not mentioned	Not mentioned
LCM	McDowell [95]	PFC; 3D; Cluster	2e9; 2e9	0.5	Not mentioned	0.7
LCM	Xiao [31, 34, 52]	PFC; 2D; Cluster	3e8; 3e8	0.5	Not mentioned	Not mentioned
LCM	Liu [35]	PFC; 3D; Clump	6.3e7; 6.3e7	0.7	Not mentioned	0.7
LCM	Khatibi [36]	PFC; 3D; Clump	4.2e7; 5.5e7	0.9	Not mentioned	Not mentioned
LCM	Zeng [37]	PFC; 3D; Clump	5.5e7; 5.5e7	0.5	Not mentioned	Not mentioned
LCM	Dahal [41]	PFC; 3D; Cluster	3e8; 3e8	0.25	Not mentioned	0.7
LCM	Mahmoud [45]	PFC; 2D; Cluster	1e11; 1e11	0.7	Not mentioned	Not mentioned
LCM	Lobo-Guerrero [46]	PFC; 2D; Ball	1e8; 1e8	0.7	Not mentioned	Not mentioned
LCM	Qian [53]	PFC; 3D; Cluster	2e6; 2e6	0.5	Not mentioned	Not mentioned
LCM	Chen [56]	PFC; 3D; Clump	5.08e9; 5.08e9	0.6	Not mentioned	Not mentioned
LCM	Kim [73]	Dynamic optimization method; 3D; Clump	9.09e6; 2.28e6	0.5	608; 304 (Ns/m)	-
LCM	Liu [65]	PFC; 3D; Cluster	5e9; 5e9	1.0	Not mentioned	1.0
LCM	Mahmoud [91]	PFC; 3D; Sphere	1.5e6; 1.5e6	0.3	Not mentioned	0.7
Contact model	Reference	Software; Particle type	Shear modulus (GPa); Poisson's ratio	Friction coefficient	Normal damping ratio; Shear damping ratio	Damping
HCM	McDowell [10]	PFC; 3D; Clump and clump & cluster	28; 0.25	0.5	Not mentioned	0.7
HCM	Gong [99]	Yade; 3D; Clump	0.15; 0.2 (Young's modulus)	0.5	Not mentioned	Not mentioned
Contact model	Reference	Software; Particle type	Shear modulus (GPa); Poisson's ratio	Friction coefficient	Rolling friction coefficient	Restitution coefficient
RRLM	Irazábal [14]	DEMPack; 3D; Sphere	5.9/11.8/17.7/23.6; 0.18	0.6	0.2/0.25/0.3	0.4

Contact model	Reference	Software; Particle type	Normal stiffness; Shear stiffness (N/m)	Friction coefficient	Normal damping ratio; Shear damping ratio	Normal damping ratio; Shear damping ratio
RRLM	Li [127]	PFC; 3D; Sphere	5e8; 5e8	0.7	0.7	0.05

Contact model	Reference	Software; Particle type	Young's modulus (GPa); Poisson's ratio	Friction coefficient	Maximal compressive strength (MPa)	Radius yielding ( $\beta$ )
CDM	Suhr [15] [19]	Yade; 3D; Clump	30.0/60.0; 0.2	0.45	600.0/2800.0	0.0154/0.0098

654

In Table 3, most of the parameters were confirmed by matching the simulation results with the test results without much explanations. For example, the friction value is obtained generally from the direct shear test or triaxial test. It is decided by the friction angle. Even though a lot of researchers think that the stiffnesses (normal and shear) are related with the Young's modulus and Poisson's ratio, however, no evidences have been confirmed in the earlier studies. Not only the friction, but also almost all the parameters were obtained based on the direct shear test or the triaxial test except the damping value. How to decide the damping value is not given clearly until now, particularly, no studies mentioned how to define the value.

#### 2.3.1.2. Models for particle creation

The contact models introduced below are in most cases applied for the ballast particle creation in DEM models (PFC), including the linear contact bond model, linear parallel bond model and flat joint model. The linear contact bond model and the linear parallel bond model have been introduced in the Section 2.2.1, which describes the particle degradation. The flat joint model was applied once for ballast particle creation in [51]. The detailed information (reference, software, parameters) is given in Table 4.

**Linear contact bond model:** The linear contact bond model (LCBM) is developed based on the linear contact model, whose dashpots are inactive (when bond existing) and the gap between two contact spheres (discs) is zero. The bond can be imagined as two springs that act at the contact point, providing constant normal and shear stiffnesses. The specific tensile and shear strengths are two parameters for the springs. The shear strength controls the shear force, and the tensile strength controls the tensile force. Particularly, the bond allows tensile forces existing at the contact of two spheres (discs) that have a gap between them.

The bond behaviour is through the infinitesimal interface, which is elastic and carries a force (no relative rotation restriction) ( $T_F$  and  $S_F$ ), as shown in Figure 6A. The bond breakage happens once the normal force (or shear force) is over the tensile strength (or shear strength). Before the bond breaks, the behaviour is linear elastic. Once the bond breaks, the behaviour is equivalent to the linear contact model.

For the application to a particle creation, the created ballast particle is crushable. Two bond parameters are set in the LCBM, i.e. tensile strength and shear strength (unit, N). When the applied normal force (or shear force) is over the tensile strength (or shear strength), the bond breaks. Afterwards, two conditions can happen, which is dependent on if the bonded spheres (or discs) are contacted. If they are not contacted, the normal and shear forces become zero. Alternatively, the linear contact model is applied at the contact. The equations for the contact force calculation after bond breakage can be found in Section 2.3.1.1 (Linear contact model).

**Linear parallel bond model:** The linear parallel bond model (LPBM) is developed based on the linear contact model, whose dashpots are inactive when a parallel bond exists. A parallel bond can be envisioned as a cement-like material placed at the contact between two spheres (or discs). The parallel bond together with the linear contact are both activated and provide forces in parallel, and the parallel bond can also provide the moment (Figure 6B).

As shown in Figure 6B, compared with the LCM, on more infinitesimal interface is added in the LPBM. The interface (parallel bond) is able to carry both force and moment. The force and moment from relative motion between two bonded spheres (discs) are developed within the parallel bond (at the bond periphery). The force and moment are limited by the prescribed bond strength (normal and shear stresses). If one stress induced by force (either normal or shear) exceeds the parallel bond strength, the parallel bond is broken. Meanwhile, the corresponding force, moment and stiffnesses are removed.

The equations for the force calculation are shown in Equation 4. In the Equation 4(a), the  $\bar{F}$  is the parallel bond force, and  $\bar{M}$  is the parallel bond moment. The linear force and dashpot force can be

found in Section 2.3.1.1, Linear contact model. In the Equation 4(c),  $\bar{M}_t$  is the twisting moment;  $\bar{M}_b$  is the bending moment;  $\bar{M}_t^{(t-1)}$  is the twisting moment of the former timestep;  $\bar{M}_b^{(t-1)}$  is the bending moment of the former timestep;  $\bar{F}_n^{(t-1)}$  is the normal force of the former timestep;  $\bar{F}_s^{(t-1)}$  is the shear force of the former timestep;  $\bar{A}$  is the cross-sectional area,  $\bar{I}$  is the moment of inertia of the parallel bond cross-section;  $\bar{J}$  is the polar moment of inertia of the parallel bond cross section; More equations on the moment calculation can be found in [82].

Equation 4 (a)  $F_c = F_l + F_d + \bar{F}$ ,  $M_c = \bar{M}$   
 (b)  $\bar{F} = -\bar{F}_n \hat{n}_c + \bar{F}_s$   
 (c)  $\bar{M} = \bar{M}_t \hat{n}_c + \bar{M}_b$   
 (d)  $\bar{F}_n = \bar{F}_n^{(t-1)} + \bar{k}_n \bar{A} \Delta \delta_n$   
 (e)  $\bar{F}_s = \bar{F}_s^{(t-1)} - \bar{k}_s \bar{A} \Delta \delta_s$   
 (f)  $\bar{M}_t = \begin{cases} 0, & 2D \\ \bar{M}_t^{(t-1)} - \bar{k}_s \bar{J} \Delta \theta_t & \end{cases}$   
 (g)  $\bar{M}_b = \bar{M}_b^{(t-1)} - \bar{k}_n \bar{I} \Delta \theta_b$

**Flat joint model:** The flat joint model (FJM) is utilised for crushable ballast particle creation in [51]. It can provide a macroscopic behaviour of partial damage by discretizing the interface into several elements (Figure 6D). The elements carry a force and moment and are either bonded or unbonded. The partial damage is presented by that the bonded elements break, and the bonds can be broken when the force exceeds the strength limitation. Before breakage, the bond behaviour is linear elastic, and after breakage (unbonded), the behaviour is the linear contact model without dashpot, as shown in Figure 6C.

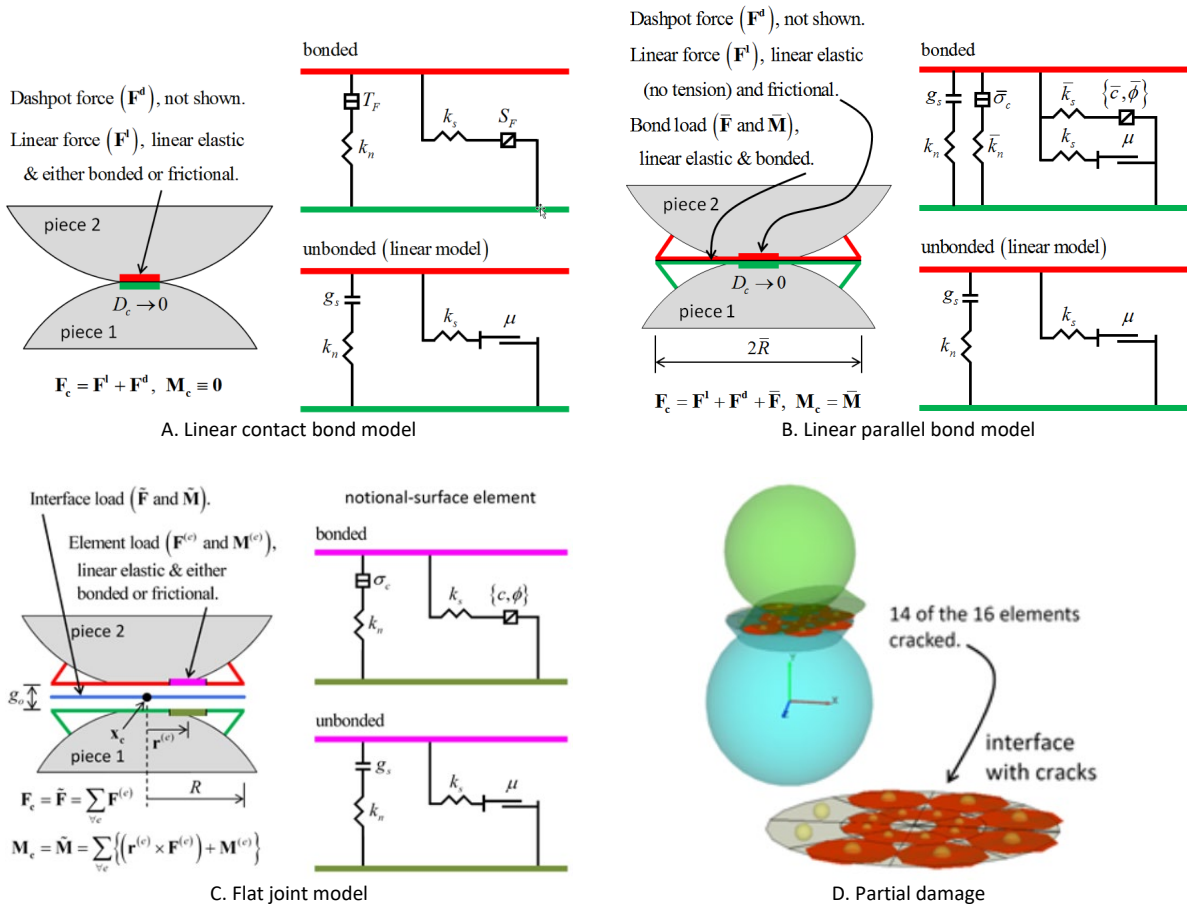


Figure 6 Contact models for particle creation (reproduced from [82])

The contact force ( $F_c$ ) and moment ( $M_c$ ) at the interface are calculated as the sum of every element force and moment ( $F^{(e)}$ ,  $M^{(e)}$ ) at the interface centre ( $X_c$ ). The element force and moment are obtained with the calculation in Equation 5. In the equation,  $F_n^{(e)}$  is the normal force;  $F_s^{(e)}$  is the shear

force;  $M_t^{(e)}$  is the twisting moment;  $M_b^{(e)}$  is the bending moment. They have the same calculation method as the parallel bond as shown in Equation 4(d)-(g).

$$\text{Equation 5 (a) } F^{(e)} = -F_n^{(e)} \hat{n}_c + F_s^{(e)}$$

$$(b) M^{(e)} = M_t^{(e)} \hat{n}_c + M_b^{(e)}$$

Table 4 Contact model for particle creation and the corresponding parameters

Contact model	Reference	Software	Parameter
LCBM	Mahmoud [45]	PFC	Contact bond: 9.42e3 kN
LCBM	McDowell [95]	PFC	Contact bond: 2.1e3 kN
LPBM	Xiao [31]; Indraratna [34]	PFC	Parallel bond: Stiffness, 6e10 N/m <sup>3</sup> ; strength 5e6 N/m <sup>2</sup> ; radius, 0.5 [31, 34]
LPBM	Indraratna [44]	PFC	Parallel bond: Stiffness, 6.25e10 N/m <sup>3</sup> ; strength, 5.78e6 N/m <sup>2</sup> ; radius, 0.5
LPBM	Indraratna [52]	PFC	Parallel bond: Stiffness, 6e10 N/m <sup>3</sup> ; strength, 5e5/5e6/5e7/5e8 N/m <sup>2</sup> ; radius, 0.5
LPBM	McDowell [30]	PFC	Parallel bond: Stiffness, 1.768e13 N/m <sup>3</sup> ; strength, 6e9 N/m <sup>2</sup> ; radius, Not mentioned
LPBM	McDowell [27]	PFC	Parallel bond: Stiffness, 1.8e13 N/m <sup>3</sup> ; strength, 5e5/5e6/5e7/5e8 N/m <sup>2</sup> ; radius, Not mentioned
LPBM	McDowell [10]	PFC	Parallel bond: Stiffness, 3.5e12 N/m <sup>3</sup> ; strength, 5e8 N/m <sup>2</sup> ; radius, 1
LPBM	Qian [53]	PFC	Parallel bond: Stiffness, 3e14 N/m <sup>3</sup> ; strength, 3e8 N/m <sup>2</sup> ; radius, 0.5
LPBM	Liu [65]	PFC	Parallel bond: Stiffness, 1.8e5 N/m <sup>3</sup> ; strength, 6e10 N/m <sup>2</sup> ; radius, 1.0 [65]
LPBM	Dahal [41]	PFC	Parallel bond: Stiffness, 6e10 N/m <sup>3</sup> ; strength, 3e7 N/m <sup>2</sup> ; radius, 0.5
LPBM	Chen [32]	PFC	Parallel bond: Shear stiffness, 5e6 N/m <sup>3</sup> ; Normal stiffness, 4e9 N/m <sup>3</sup> ; strength, 3e7 N/m <sup>2</sup> ; radius, not mentioned
FJM	Wang [51]	PFC	Element number: 3; bond strength: 6e6/10e6/12.5e6 N/m <sup>2</sup> ; Cohesion: 12e6/100e6/28e6 N/m <sup>2</sup>

In Table 4, most of the parameter values are confirmed based on the single particle crush test, specifically, matching the load-stress curve of simulations with that of the experiments and fitting the Weibull distribution. Even so, the radius is still a value that needs further study due to it is defined as a value without many explanations.

### 2.3.2. Basic element non-sphere

Due to different models with non-sphere particles are developed by different researchers, the contact models are not the same. For example, for the spring-dashpot model, different algorithms for the contact force computation can be given, although all their contact forces are calculated by the product of the stiffness and the overlap increment.

**Linear contact model:** The linear contact model used in the Block3D allows the particle overlap at the contact point, and the contact forces are calculated at every contact points. The equations for contact force ( $F_c$ ) calculation are given in Equation 6. In the equations,  $F_n$  is the normal force;  $F_s$  is the shear force;  $F_n^{(e)}$  is the elastic force;  $F_n^{(d)}$  is the damping force;  $k_n$ ,  $k_{nn}$  and  $b$  are constant parameters for materials;  $D_n$  is the average penetration distance;  $k_s$  is the contact shear stiffness;  $U_n$  and  $U_s$  are the relative displacement increment at normal and shear directions, respectively. If  $k_{nn}$  is set as 0, the contact is typical linear force-displacement model; if  $k_n$  is set as 0 and proper values are given to  $k_{nn}$  and  $b$ , the contact is Hertzian contact model.

$$\text{Equation 6 (a) } F_c = F_n + F_s$$

$$(b) F_n = F_n^{(e)} + F_n^{(d)}$$

$$(c) F_s = F_s^{(e)} + F_s^{(d)}$$

$$(d) F_n^{(e)} = k_n D_n + k_{nn} (D_n)^b$$

$$(e) F_s^{(e)} = \left( F_s^{(e; t-1)} - \left( F_s^{(e; t-1)} \cdot n^t \right) n^t \right) + k_s \Delta U_s^t$$

$$(f) F_n^{(d)} = \beta_a k_{ln} \dot{U}_n$$

$$(g) F_s^{(d)} = \beta_a k_s \dot{U}_s$$

**Hertz contact model:** The Hertzian contact model in [33] applies the modified Mindlin and Deresiewicz theory, and it treats the contact between two particles as two ellipsoids' contact (elliptic contact area) [128]. Afterwards, the equivalent sphere with radius ( $R_c$ ) is calculated by the Equation 7(a). In the equation,  $R_a$  and  $R_b$  are calculated with Equation 6(b-e), and  $\kappa_{11}$  is the first particle major principal curvatures;  $\kappa_{12}$  is the minor principal curvatures;  $\alpha$  is the angle of two particles' major and minor curvature relative rotation. The normal force can be calculated with the Equation 6(f).  $\delta$  is the overlap, and  $k_n$  is expressed as Equation 6(g).  $E$ ,  $G$  and  $\nu$  are Young's modulus, shear modulus and Poisson's ratio, respectively.

$$\begin{aligned}
\text{Equation 7 (a)} \quad R_c &= \sqrt{R_a R_b} \\
\text{(b)} \quad R_a &= 1/((A + B) - (B - A)) \\
\text{(c)} \quad R_b &= 1/((A + B) + (B - A)) \\
\text{(d)} \quad A + B &= (\kappa_{11} + \kappa_{12} + \kappa_{21} + \kappa_{22})/2 \\
\text{(e)} \quad B - A &= \frac{1}{2} \sqrt{(\kappa_{11} - \kappa_{12})^2 + (\kappa_{21} - \kappa_{22})^2 + 2(\kappa_{11} - \kappa_{12})(\kappa_{21} - \kappa_{22}) \cos(2\alpha)} \\
\text{(f)} \quad F_n &= k_n \delta \\
\text{(g)} \quad k_n &= \frac{4}{3} E_c \left( \frac{R_c \delta}{F_n^2} \right)^{1/2} \\
\text{(h)} \quad \frac{1}{E_c} &= \frac{1-\nu_1^2}{E_1} + \frac{1-\nu_2^2}{E_2} = \frac{1-\nu_1}{2G_1} + \frac{1-\nu_2}{2G_2} \\
\text{(i)} \quad F_2 &\cong 1 - \left[ \left( \frac{R_a}{R_b} \right)^{0.0684} - 1 \right]^{1.531}
\end{aligned}$$

For the shear contact force, the initial (or maximum) shear stiffness is calculated with the Equation 8(a).  $G_c$  is the contact shear modulus expressed by Equation 8(b). Two factors,  $\Phi$  and  $F_1$ , are related to the eccentricity of the contact area.

$$\begin{aligned}
\text{Equation 8 (a)} \quad k_s &= 8G_c F_1 \left( \frac{3R_c R_a F_n}{4E_c R_b} \right)^{1/3} \frac{1}{\Phi} \\
\text{(b)} \quad \frac{1}{G_c} &= \frac{2-\nu_1}{G_1} + \frac{2-\nu_2}{G_2} \\
\text{(c)} \quad F_1 &\cong 1 - \left[ \left( \frac{R_a}{R_b} \right)^{0.0602} - 1 \right]^{1.456} \\
\text{(d)} \quad \Phi &\cong \begin{cases} 1 + (1.4 - 0.8\nu) \log \left[ \left( \frac{R_a}{R_b} \right)^{2/3} \right] & R_a < R_b \\ 1 & R_a = R_b \\ 1 + (1.4 + 0.8\nu) \log \left[ \left( \frac{R_a}{R_b} \right)^{2/3} \right] & R_a > R_b \end{cases}
\end{aligned}$$

**Conical damage model:** The conical damage model (CDM) treats the contact as asperity on a sphere or a plane, and the asperity can have conical damage. The damage is presented by asperity radius increases, as shown in Figure 3C [28]. The asperity is ideally represented as a cone, and the angle  $\alpha$  is made by the cone side and the vertical (Figure 3C). Moreover, the asperity has an apex that is with curvature radius ( $R$ ), and the curvature radius  $R_{min}$  can be obtained (Figure 3C). The maximum stress ( $\sigma_0$ ) is given in Equation 9(a). In the equation,  $R$  is the contact area radius;  $P$  is the normal force;  $\delta$  is the overlap. When the acting stress is over the material ultimate strength ( $\sigma_{cmax}$ ), the contact cannot bear the force ( $P_{max}$ ). Towards this, the  $\sigma_0$  is set equal to  $\sigma_{cmax}$ , then the new contact area radius  $R$  can be obtained as shown in Equation 9(c).

Afterwards, the asperity is replaced by a more rounded cap. The offset of the cap ( $\delta_c$ ) is calculated with Equation 9(d). The updated normal force ( $P$ ) is obtained according to the updated overlap ( $\delta$ ), and a new contact stiffness  $k_n$  is applied (Equation 9(e)(f)), which is updated based on the contact area radius  $R$ . In addition, the updated shear stiffness is calculated with Equation 9(g).

$$\begin{aligned}
\text{Equation 9 (a)} \quad \sigma_0 &= \frac{3P}{2\pi R \delta} = \frac{1}{\pi} \left( \frac{6PE^2}{R^2} \right)^{1/3} \\
\text{(b)} \quad \frac{1}{E^*} &= \frac{1-\nu_1}{2G_1} + \frac{1-\nu_2}{2G_2} \\
\text{(c)} \quad R &= \frac{E^* \sqrt{6P_{max}}}{(\pi \sigma_{cmax})^{3/2}} \\
\text{(d)} \quad \delta_c &= R \left( \frac{1 - \sin(\alpha)}{\sin(\alpha)} \right) \\
\text{(e)} \quad P &= k_n \delta
\end{aligned}$$



$$(f) k_n = \frac{4}{3} E^* \sqrt{R\delta}$$

$$(g) k_s = \frac{4}{3} k_n E^* \sqrt{R}$$

**Non-smooth contact dynamics:** The Non-smooth contact dynamics (NSCD) is developed using the “Non-smooth” methods and assumes that the contacts between particles are perfectly rigid. In other words, no deformation or overlap is allowed at the contact between particles, however, the particle is able to have deformation. The “Non-smooth” means that the relationship of the normal force and normal motion is based on non-smooth mutual exclusion formulation. The contact law is Signorini-Coulomb law is applied using the implicit time integration and dray friction between particles. Moreover, the restitution coefficient is used deciding the particle velocity after acted by a contact force, which can reflect the kinetic energy dissipation during the calculation. The advantage of this contact law is that it allows large time steps [129].

The equations for the force-displacement law are given in Equation 10. In the equations,  $g$  is the gap of the two adjacent particles;  $F_n$  is the normal force;  $V_n$  is the relative particle normal velocity;  $k_n$  is the stiffness;  $F_t$  is the shear force;  $V_t$  is the relative particle normal velocity;  $\mu$  is the friction. The relative movements happen only when the shear force is over the value of  $\mu \cdot F_n$ . More descriptions on the dynamic equations and contact law can be found in [110, 130].

$$\text{Equation 10 (a) when } g \leq 0, \text{ then } \begin{cases} F_n \geq 0; V_n \geq 0 \\ F_n \cdot V_n = 0 \end{cases}$$

$$(b) F_n = -k_n \cdot g$$

$$(b) \begin{cases} \|dF_t\| \leq \mu \cdot dF_n, \text{ if } V_t = 0 \\ dF_t = -\mu \cdot \frac{dF_n}{\|dF_n\|}, \text{ if } V_t \neq 0 \end{cases}$$

**Volume-based contact model:** the volume-based contact model is developed by Elias in [112], which calculates the normal force linearly based on the inserted volume (overlap) between two particles. Equation 11 describes the calculation method for contact force. In the Equation 11(a),  $V_I$  is the overlap volume;  $k_n$  is the volumetric stiffness (unit, N/m<sup>3</sup>). Afterwards, the method for overlap volume calculation can be found in [112]. Equation 11(b) presents how to calculate the shear force. In the equation,  $\Delta\mu_s$  is the additional shear displacement increment;  $k_s$  is the shear stiffness (N/m).

$$\text{Equation 11 (a) } |F_n| = V_I k_n$$

$$(b) \Delta F_s = \Delta\mu_s k_s$$

Table 5 Contact model for basic element non-sphere

Contact model	Reference	Software	Parameters			
LCM	Bian [22]	BLOKS3D	Normal contact stiffness (N/m): 2e6	Shear contact stiffness (N/m): 1e6	Surface friction angle (degree): 31	Contact damping: 0.2
LCM	Qian [11]; Tutumluur [42]	BLOKS3D	Normal contact stiffness (N/m): 2e6	Shear contact stiffness (N/m): 1e6	Surface friction angle (degree): 31	Contact damping: 0.4
LCM	Qian [29, 116]	BLOKS3D	Normal contact stiffness (N/m): 2e6	Shear contact stiffness (N/m): 1e6	Surface friction angle (degree): 31	Global damping: 0.06 Contact damping: 0.03
HCM	Ahmed [33]	Not mentioned	Contact stiffness (GPa): 1.0	Poisson's ration: not-mentioned	Friction angle (degree): 30/35/40	Damping: 0.5
HCM	Ji [43, 113]	Not mentioned	Shear modulus (GPa): 20	Poisson's ration: 0.3	Coefficient of restitution: 0.8	Friction: 0.5
CDM	Harkness [28]	Not mentioned	Shear modulus (GPa): 10.0/5.0/1.0/0.5	Poisson's ration: 0.2	Friction angle (degree): 20/30/40	-
NSCD	Saussine [68, 110, 129, 131]	LMGC90	Friction: 0.5/0.8/1.0	-	-	-
VBCM	Eliáš [112]	Yade	Normal volumetric	Shear stiffness	Friction angle (rad):	Damping: 0.3

### 2.3.3. Discussion

1. Most of the ballast studies using the DEM applied the PFC as the tool, and the linear contact model is the most popular one. In the linear contact model of PFC, the contact damping (dashpot) is usually set to 0, and the local damping (i.e. restitution coefficient) is applied with the default value 0.7 in most cases. The value has not been carefully validated, possibly, it is acceptable in the static or quasi-static condition (e.g. direct shear test). However, when it comes to the dynamic condition (cyclic loading), especially the conditions containing impact loading (e.g. tamping), the damping value (contact damping, local damping) is crucial and needs carefully calibrated.
2. Most of the DEM studies utilise the overlapped between two particles to calculate contact forces. For this, the contact stiffness values (normal and shear directions) are important, interestingly, in the LCM the contact stiffness value varies from 5e5 to 1e9 with a large difference. In addition, the normal stiffness and shear stiffness are usually set as a same value. Even though the contact stiffness is assumed to have the correlation with the ballast material strength, it is not possible to make this large difference. Therefore, the value should be checked and confirmed with experimental tests according to the ballast material strength.
3. Ballast material does not allow large deformation at the contact. Consequently, most of the DEM should use a very small timestep and very high contact stiffness value for correctly dealing with the big contact rigidity. This can lead to a long computation time. Therefore, more optimisation studies on this direction should be performed.
4. Even though the linear contact model is the most widely-used contact model, the other models or model improvement are still necessary for better calibration. Consequently, the comparison of different contact models is necessary for choosing accurate contact model, which to date has not been found in any literature of railway ballast. For example, the comparison can be performed among the linear contact bond model, parallel bond model and the flat joint model, and also between the linear contact model and the Hertz contact model.
5. More importantly, the models in PFC are mostly based on the linear contact model, e.g. the rolling resistance linear contact model. Two aspects can be improved. On one hand, the twisting resistance could also be considered in 3D models. On the other hand, the models can be developed based on the Hertz contact model.
6. In practise, the friction should not be a constant value, and it changes as many situations, e.g. wet or dry and contact means (face-face, aspect-face). In addition, the friction can increase as the normal force. Therefore, developing new algorithm for this is a research direction.
7. New contact model can be developed for railway ballast based on a new theory, which can lead to more similar performance as railway ballast interactions. More importantly, the new models should be calibrated with the consideration of the particle type (sphere-based or polyhedron) particle shape and size.
8. The Non-smooth contact dynamics is a suitable contact method for ballast simulations. However, a disadvantage is that this contact method is lack of contact elasticity. In other words, at the contact area has no deformation, which is not realistic and can cause the error accumulation of the condition under the cyclic loadings, particularly, when the long-term performance of ballast particles is analysed.
9. In all the contact models, the parameters are calibrated with the experimental tests, and in most cases the static or quasi-static tests are utilised. The only indicator (dynamic test) applied in the earlier studies is the deformation of ballast assemblies. For this, the parameters are confirmed from the macro-level instead of the meso-level. It needs to note that the contacts between ballast particles are at the meso-level, therefore, experimental tests should be designed for accurate contact model calibration.

## 3. Summary, conclusions and perspectives

### 3.1. Summary

In this paper, three aspects of DEM model calibration (for ballast) are introduced and the earlier studies are summarised and explained in details in the tables. The three calibration aspects include the morphology (size and shape), ballast particle degradation (breakage and abrasion) and the contact model (particle interaction). In each aspect, the calibration methods are firstly introduced, afterwards, the discussions are given.

Regarding the morphology calibration, how the ballast particles are modelled more realistic is introduced. In this aspect, due to the basic elements are different in different software, the particle calibration method is different. The particle generation methods (algorithms) are introduced. For the sphere (disc), clump, cluster or clump & cluster are the widely-used method, which is to use more spheres (discs) to model one ballast particle. For the polyhedron (polygon), the image-based method is the most common one.

Concerning the ballast particle degradation calibration, how to present ballast particle degradation is introduced. For the sphere (disc), two methods for particle breakage are developed, i.e. bonded-particle model and the fragment replacement method. The abrasion is presented by releasing small sphere/disc from the main particle, or increasing the radius of the sphere that is at the position of the edge or corner. For the polyhedron (polygon), the fragment replacement method is applied to present breakage, and the abrasion is presented by through a new contact model, conical damage model.

For the contact model, the contact models (algorithms) are introduced and the values of the corresponding parameters are summarised in tables. For the sphere (disc), two types of contact models are introduced, i.e. models for particle interaction and models for particle creation. For the polyhedron (polygon), the contact models are not exactly the same due to the algorithms are developed by different researchers.

Based on the discussions in each aspect, the following conclusions and perspectives are given.

### 3.2. Conclusions

Based on the above introductions and discussions, the suitable recommendations for some certain applications are given in this section. This is able to help choose the most suitable model with calibrated parameters for the certain situations. The recommendations are given according to the search problems mentioned in the Introduction, i.e. 1) performance evaluation, 2) ballast bed degradation mechanism, 3) ballast degradation mitigation and performance improvement and 4) maintenance.

#### 3.2.1. Performance evaluation

For the performance evaluation, several models of laboratory tests (direct shear test, triaxial test) or field tests (single sleeper push test, sleeper supporting condition) are used to analyse the durability, stability, shear strength, stiffness and resilience, as well as the factors influencing the performance, such as particle shape, particle size distribution.

The direct shear test (DST) is a commonly used for testing the shear strength of ballast assemblies or for parameter confirmation. In recent studies, how the morphology influences the shear strength is dug in depth as a research hotspot [132-135]. For the morphology calibration, the more complex particles are recommended, such as the clump with around 20 spheres/discs (Table 1; No. 13), due to 1) the DST is generally at the meso-level (e.g. particle interaction and interlocking), 2) the ballast sample is small (e.g. 300\*300\*400 mm), 3) the calculation process (displacement at centimetre level) is much short than other tests (e.g. tests with cyclic loadings) and 4) ballast degradation is relatively not obvious during the DST. For the degradation calibration, it is not necessary to consider the ballast degradation in the DST models, because the degradation is not obvious according to the experimental experiences [124]. For the contact model calibration, all the contact models are almost

the same due to the simulating process is very short only within 10 cm. The influences of choosing different contact models on the results are not obvious. However, for the parameters in each model, the recommendations are not easy to given due to the differences between real contact and the simulated contact, which needs considerably more studies.

The single sleeper push test model is used for confirming the track stability, and the corresponding studies focus on the sleeper shape effects, contribution of different ballast components and application of geo-inclusions [136]. It has similar conditions as the DST model, therefore, the recommendations are the same. Specifically, for the morphology calibration, the clump with at least 20 spheres/discs (Table 1; No. 13) is recommended. Moreover, it is not necessary to consider the ballast degradation in this test, because almost no breakages or abrasions happen during the test process. All the contact models provide almost the same results, however, confirming the parameters in each contact model should be focused on more until reliable and convincing ones are given, which are obtained from the real test contact conditions, e.g. the study in [137].

The triaxial test has two types of tests, i.e. triaxial test and cyclic triaxial test. For the triaxial test model, it is almost the same situation as the DST model, while the cyclic triaxial test model is much more different. Due to the cyclic loadings, the computation cost of the simulation process is huge, therefore, the calibration is dependent on the focused study questions. For example, to reduce the computation cost for more loading cycles, the 2D clump can be used when the degradation is not involved. In the conditions that the degradation is necessary, the 2D clump & cluster (Table 1, No. 9) or cluster (Table 1, No. 5) can be used. The degradation calibration is necessary for the cyclic triaxial test models, and the FJM (Table 4) is suitable until now for the single particle crush. The LPBM or LCBM are recommended, however, more developments on creating new fast contact models for particle creation are of importance. When it comes to the contact models for particle interaction, the HCM is more promising than the LCM (Table 3). This is due to the HCM can present the influences of particle size on the contact forces (Equation 7), and the LCM possibly produces errors because of the residual force accumulations.

### 3.2.2. Ballast bed degradation mechanism

The ballast bed degradation mechanism at some special railway structures can be studied with the DEM models, such as, turnouts and transition zones. It is urgent due to the demand of higher train speed and heavier axle load, for example, in China the train speed is over 350 km/h. Until now, the turnout models are built with the Finite Element Method (FEM) or multi-body dynamics [138-140], which is lack of ballast analysis. however, the ballast conditions significantly affect the turnout performance. The DEM models can be built to analyse the ballast rearrangements and degradation. Due to the impact loading at turnouts is not only at the longitudinal and vertical directions, but also the lateral directions, it is considerably interesting to demonstrate the ballast rearrangements and degradation under this loading condition. Because the turnout model should at least have five sleepers and the rearrangements are mainly focused on, therefore, using the spheres are recommended with the RRLM (Figure 4C). The degradation calibration can use the method in Figure 2A. Particularly, the method can have an improvement, which is changing the sphere into several clumps to present breakage.

For the transition zones, the coupled DEM-FEM models are becoming popular [141]. However, the computation cost remains a big problem, even though in [142] the 2D clusters (Table 1; No. 6) are applied and the subgrade is built with the FEM. Generally, the transition zone studies focus on balancing the stiffness difference of the bridge side and the subgrade side. In this case, for reducing the computation cost and increasing the loading cycles, the clumps are recommended. Alternatively, the discs with the RRLM (Figure 4C) can also be applied. However, it needs to note that the 2D models are usually with errors due to the lateral direction is omitted. Because ballast particle movements at the lateral direction are one reason to the ballast bed settlement.

### 3.2.3. Ballast degradation mitigation and performance improvement

To reduce ballast degradation mitigation and improve performance, new materials are applied in the ballast layer, such as, the under sleeper pads, geogrid, geocell and polyurethane. Due to the different research goals, the DEM models for these applications of new materials are different. Specifically, for the new materials, using the DEM for settlement and ballast degradation analysis in cyclic triaxial test models (or other small-scale laboratory test models) can choose the 2D clusters (Table 1; No. 4, 5). Due to the sharp corner loss is the main degradation type, the clump & cluster (Table 1; No. 9) can also be used, which can present the ballast abrasion (Figure 3). For the contact model, the HCM is also recommended with properly calibrated damping. Alternatively, using the DEM for large scale track model simulations (over three sleepers) can choose the 3D sphere or 2D clump. This is due to the spheres with proper contact model can also present similar performance (e.g. lateral resistance), and this can considerably save time. In addition, the degradation can also be considered using the methods in Table 2 (No. 4, 5). The contact model of the RRLM (Figure 4C) can be used or other contact models have not been applied in ballast studies, e.g. rolling and twisting resistance contact model in [143].

### 3.2.4. Maintenance

The tamping process can be simulated with the clump, cluster or clump & cluster (Table 1; No. 8, 9, 13) for different situations. Specifically, the clump is suitable for testing the performance after tamping, e.g. lateral resistance, particle rearrangement study. The cluster or clump & cluster can be used when the ballast particle degradation is mainly focused on. It needs to note that only 3D is recommended in this case, because the particle rearrangements during the tamping are big, including at the lateral direction. More importantly, due to ballast particle degradation (breakage and abrasion) is relatively severer than other situations (cyclic loading), therefore, it is better to consider the ballast particle degradation (especially breakage) in the DEM models, e.g. methods in Table 2 (No. 3, 4, 6). Until now, the contact models (including the parameters in the contact models) are not well calibrated, due to the rapid impact loading is the normal loading. The particle breakage and relative motion (shaking) can cost very large kinetic energy, and the abrasion (wear) is not easy to present with current contact models.

## 3.3. Perspectives

1. Morphology: particle size distribution is the only means for size not only in the laboratory or field tests, but also in the DEM models. Presenting the same PSD with the tests are rarely, therefore, size can be calibrated with this method to improve the model accuracy.
2. Degradation: limited studies were found on how to present angularity loss or polygon breaks, moreover, no studies until now were found on presenting surface texture reduction. More importantly, it is necessary to consider the ballast material, inner crack and surface crack. Therefore, combining all the factors are encouraged in the future studies.
3. Contact model: the contact models are not fully validated in dynamic conditions. More studies should be performed on the energy dissipation part, e.g. new contact model development. Due to the improper energy dissipation, the error accumulation can lead to wrong simulation results.
4. Until now, the calibration aspects are separated in each study. In other words, only one aspect usually is considered in one study. Considering the three aspects together in one study can be more realistic when calibrating the DEM models.

## Acknowledgements

The research is supported by the China Scholarship Council and the Natural Science Foundation of China (Grant No. 51578469). We also would like to acknowledge the support of the Chinese Program of Introducing Talents of Discipline to Universities (111 Project, Grant No. B16041). We want to thank the support during the work at the International Joint Laboratory of Railway System Dynamics in Southwest Jiaotong University, established by the Chinese Ministry of Education.

## Reference

- [1] W. Zhai, K. Wang, C. Cai, Fundamentals of vehicle–track coupled dynamics, *Vehicle System Dynamics* 47(11) (2009) 1349-1376.
- [2] D. Li, J. Hyslip, T. Sussmann, S. Chrismer, *Railway geotechnics*, CRC Press 2002.
- [3] B. Indraratna, W. Salim, C. Rujikiatkamjorn, *Advanced rail geotechnology: Ballasted track*, CRC press London 2011.
- [4] W. Zhai, K. Wang, J. Lin, Modelling and experiment of railway ballast vibrations, *Journal of sound and vibration* 270(4) (2004) 673-683.
- [5] W. Zhai, *Vehicle–Track Coupled Dynamics: Theory and Applications*, Springer Nature 2019.
- [6] A. Danesh, M. Palassi, A.A. Mirghasemi, Evaluating the influence of ballast degradation on its shear behaviour, *International Journal of Rail Transportation* 6(3) (2018) 145-162.
- [7] D. Gundavaram, S.K.K. Hussaini, Polyurethane-based stabilization of railroad ballast—a critical review, *International Journal of Rail Transportation* 7(3) (2019) 219-240.
- [8] X. Zhang, C. Zhao, W. Zhai, Dynamic Behavior Analysis of High-Speed Railway Ballast under Moving Vehicle Loads Using Discrete Element Method, *International Journal of Geomechanics* 17(7) (2016) 04016157.
- [9] G. Jing, H. Fu, P. Aela, Lateral displacement of different types of steel sleepers on ballasted track, *Construction and Building Materials* 186 (2018) 1268-1275.
- [10] H. Li, G.R. McDowell, Discrete element modelling of under sleeper pads using a box test, *Granular Matter* 20(2) (2018).
- [11] Y. Qian, E. Tutumluer, Y.M.A. Hashash, J. Ghaboussi, D.D. Davis, Ballast Settlement Ramp to Mitigate Differential Settlement in a Bridge Transition Zone, *Transportation Research Record: Journal of the Transportation Research Board* 2476(2476) (2015) 45-52.
- [12] P.A. Cundall, O.D. Strack, A discrete numerical model for granular assemblies, *geotechnique* 29(1) (1979) 47-65.
- [13] C. O'Sullivan, *Particulate discrete element modelling: a geomechanics perspective*, CRC Press 2014.
- [14] J.I. González, Numerical analysis of railway ballast behaviour using the Discrete Element Method, *Universitat Politècnica de Catalunya*, 2017.
- [15] B. Suhr, S. Marschnig, K. Six, Comparison of two different types of railway ballast in compression and direct shear tests: experimental results and DEM model validation, *Granular matter* 20(4) (2018) 70.
- [16] D. Mishra, S.N. Mahmud, Effect of Particle Size and Shape Characteristics on Ballast Shear Strength: A Numerical Study Using the Direct Shear Test, 2017 Joint Rail Conference, American Society of Mechanical Engineers, 2017, pp. V001T01A014-V001T01A014.
- [17] Z. Wang, G. Jing, Q. Yu, H. Yin, Analysis of ballast direct shear tests by discrete element method under different normal stress, *Measurement* 63 (2015) 17-24.
- [18] H. Huang, E. Tutumluer, Discrete Element Modeling for fouled railroad ballast, *Construction and Building Materials* 25(8) (2011) 3306-3312.
- [19] B. Suhr, K. Six, Parametrisation of a DEM model for railway ballast under different load cases, *Granular Matter* 19(4) (2017) 64.
- [20] B. Indraratna, S.S. Nimbalkar, N.T. Ngo, T. Neville, Performance improvement of rail track substructure using artificial inclusions – Experimental and numerical studies, *Transportation Geotechnics* 8 (2016) 69-85.
- [21] B. Indraratna, N.T. Ngo, C. Rujikiatkamjorn, J. Vinod, Behavior of fresh and fouled railway ballast subjected to direct shear testing: discrete element simulation, *International Journal of Geomechanics* 14(1) (2012) 34-44.
- [22] X. Bian, W. Li, Y. Qian, E. Tutumluer, Micromechanical Particle Interactions in Railway Ballast through DEM Simulations of Direct Shear Tests, *International Journal of Geomechanics* 19(5) (2019).
- [23] S. Laryea, M. Safari Baghsorkhi, J.F. Ferrellec, G.R. McDowell, C. Chen, Comparison of performance of concrete and steel sleepers using experimental and discrete element methods, *Transportation Geotechnics* 1(4) (2014) 225-240.
- [24] M. Lu, G.R. McDowell, The importance of modelling ballast particle shape in the discrete element method, *Granular Matter* 9(1-2) (2006) 69-80.
- [25] M. Lu, G. McDowell, Discrete element modelling of ballast abrasion, *Géotechnique* 56(9) (2006) 651-655.
- [26] C. Chen, G.R. McDowell, N.H. Thom, Discrete element modelling of cyclic loads of geogrid-reinforced ballast under confined and unconfined conditions, *Geotextiles and Geomembranes* 35 (2012) 76-86.
- [27] G.R. McDowell, H. Li, Discrete element modelling of scaled railway ballast under triaxial conditions, *Granular Matter* 18(3) (2016).
- [28] J. Harkness, A. Zervos, L. Le Pen, S. Aingaran, W. Powrie, Discrete element simulation of railway ballast: modelling cell pressure effects in triaxial tests, *Granular Matter* 18(3) (2016) 1-13.
- [29] Y. Qian, D. Mishra, E. Tutumluer, H.A. Kazmee, Characterization of geogrid reinforced ballast behavior at different levels of degradation through triaxial shear strength test and discrete element modeling, *Geotextiles and Geomembranes* 43(5) (2015) 393-402.
- [30] M. Lu, G.R. McDowell, Discrete element modelling of railway ballast under monotonic and cyclic triaxial loading, *Géotechnique* 60(6) (2010) 459-467.
- [31] J. Xiao, D. Zhang, K. Wei, Z. Luo, Shakedown behaviors of railway ballast under cyclic loading, *Construction and Building Materials* 155 (2017) 1206-1214.
- [32] C. Chen, B. Indraratna, G. McDowell, C. Rujikiatkamjorn, Discrete element modelling of lateral displacement of a granular assembly under cyclic loading, *Computers and Geotechnics* 69 (2015) 474-484.
- [33] S. Ahmed, J. Harkness, L. Le Pen, W. Powrie, A. Zervos, Numerical modelling of railway ballast at the particle scale, *International Journal for Numerical and Analytical Methods in Geomechanics* 40(5) (2016) 713-737.
- [34] B. Indraratna, P.K. Thakur, J.S. Vinod, Experimental and numerical study of railway ballast behavior under cyclic loading, *International Journal of Geomechanics* 10(4) (2009) 136-144.
- [35] S. Liu, T. Qiu, Y. Qian, H. Huang, E. Tutumluer, S. Shen, Simulations of large-scale triaxial shear tests on ballast aggregates using sensing mechanism and real-time (SMART) computing, *Computers and Geotechnics* 110 (2019) 184-198.
- [36] F. Khatibi, M. Esmaeili, S. Mohammadzadeh, DEM analysis of railway track lateral resistance, *Soils and Foundations* 57(4) (2017) 587-602.
- [37] Z. Zeng, S. Song, W. Wang, H. Yan, G. Wang, B. Xiao, Ballast bed resistance characteristics based on discrete-element modeling, *Advances in Mechanical Engineering* 10(6) (2018) 1687814018781461.
- [38] E. Tutumluer, H. Huang, Y. Hashash, J. Ghaboussi, Aggregate shape effects on ballast tamping and railroad track lateral stability, AREMA Annual Conference, Louisville, KY, Sept, 2006, pp. 17-20.
- [39] G. Jing, P. Aela, H. Fu, The contribution of ballast layer components to the lateral resistance of ladder sleeper track, *Construction and Building Materials* 202 (2019) 796-805.
- [40] D. Nishiura, H. Sakai, A. Aikawa, S. Tsuzuki, H. Sakaguchi, Novel discrete element modeling coupled with finite element method for investigating ballasted railway track dynamics, *Computers and Geotechnics* 96 (2018) 40-54.
- [41] B. Dahal, S.N. Mahmud, D. Mishra, Simulating Ballast Breakage Under Repeated Loading Using the Discrete Element Method, 2018 Joint Rail Conference, American Society of Mechanical Engineers, 2018, pp. V001T01A003-V001T01A003.



- [42] E. Tutumluer, Y. Qian, Y.M.A. Hashash, J. Ghaboussi, D.D. Davis, Discrete element modelling of ballasted track deformation behaviour, *International Journal of Rail Transportation* 1(1-2) (2013) 57-73.
- [43] S. Ji, S. Sun, Y. Yan, Discrete element modeling of dynamic behaviors of railway ballast under cyclic loading with dilated polyhedra, *International Journal for Numerical and Analytical Methods in Geomechanics* 41(2) (2017) 180-197.
- [44] N.T. Ngo, B. Indraratna, C. Rujikiatkamjorn, Simulation Ballasted Track Behavior: Numerical Treatment and Field Application, *International Journal of Geomechanics* 17(6) (2016) 04016130.
- [45] E. Mahmoud, A.T. Papagiannakis, D. Renteria, Discrete Element Analysis of Railway Ballast under Cycling Loading, *Procedia Engineering* 143 (2016) 1068-1076.
- [46] S. Lobo-Guerrero, L.E. Vallejo, Discrete Element Method Analysis of Railtrack Ballast Degradation during Cyclic Loading, *Granular Matter* 8(3-4) (2006) 195-204.
- [47] S. Liu, H. Huang, T. Qiu, L. Gao, Comparison of Laboratory Testing Using SmartRock and Discrete Element Modeling of Ballast Particle Movement, *Journal of Materials in Civil Engineering* 29(3) (2017) D6016001.
- [48] I. Deiros, C. Voivret, G. Combe, F. Emeriault, Quantifying Degradation of Railway Ballast Using Numerical Simulations of Micro-deval Test and In-situ Conditions, *Procedia Engineering* 143 (2016) 1016-1023.
- [49] H. Huang, S. Chrismer, Discrete element modeling of ballast settlement under trains moving at "Critical Speeds", *Construction and Building Materials* 38 (2013) 994-1000.
- [50] W.T. Hou, B. Feng, W. Li, E. Tutumluer, Ballast Support Condition Affecting Crosstie Performance Investigated through Discrete Element Method, *Pr Asme Joint Rail C* (2018).
- [51] B. Wang, U. Martin, S. Rapp, Discrete element modeling of the single-particle crushing test for ballast stones, *Computers and Geotechnics* 88 (2017) 61-73.
- [52] P. Thakur, J.S. Vinod, B. Indraratna, Effect of particle breakage on cyclic densification of ballast: A DEM approach, *IOP Conference Series: Materials Science and Engineering*, IOP Publishing, 2010, p. 012229.
- [53] J. Qian, J. Gu, X. Gu, M. Huang, L. Mu, DEM Analysis of Railtrack Ballast Degradation under Monotonic and Cyclic Loading, *Procedia Engineering* 143 (2016) 1285-1292.
- [54] Z. Hossain, B. Indraratna, F. Darve, P. Thakur, DEM analysis of angular ballast breakage under cyclic loading, *Geomechanics and Geoengineering: An International Journal* 2(3) (2007) 175-181.
- [55] E. Tutumluer, H. Huang, Y. Hashash, J. Ghaboussi, Discrete element modeling of railroad ballast settlement, AREMA conference, 2007.
- [56] C. Chen, G.R. McDowell, An investigation of the dynamic behaviour of track transition zones using discrete element modelling, *Proceedings of the Institution of Mechanical Engineers, Part F: Journal of Rail and Rapid Transit* 230(1) (2014) 117-128.
- [57] C. Chen, G.R. McDowell, N.H. Thom, A study of geogrid-reinforced ballast using laboratory pull-out tests and discrete element modelling, *Geomechanics and Geoengineering* 8(4) (2013) 244-253.
- [58] B. Indraratna, S. Nimbalkar, C. Rujikiatkamjorn, From theory to practice in track geomechanics – Australian perspective for synthetic inclusions, *Transportation Geotechnics* 1(4) (2014) 171-187.
- [59] S.N. Mahmud, D. Mishra, D.O. Potyondy, Effect of Geogrid Inclusion on Ballast Resilient Modulus: The Concept of 'Geogrid Gain Factor', 2018 Joint Rail Conference, American Society of Mechanical Engineers, 2018, pp. V001T01A005-V001T01A005.
- [60] Y. Qian, E. Tutumluer, H. Huang, A validated discrete element modeling approach for studying geogrid-aggregate reinforcement mechanisms, *Geo-Frontiers 2011: Advances in Geotechnical Engineering 2011*, pp. 4653-4662.
- [61] N.T. Ngo, B. Indraratna, C. Rujikiatkamjorn, Modelling geogrid-reinforced railway ballast using the discrete element method, *Transportation Geotechnics* 8 (2016) 86-102.
- [62] N.T. Ngo, B. Indraratna, C. Rujikiatkamjorn, DEM simulation of the behaviour of geogrid stabilised ballast fouled with coal, *Computers and Geotechnics* 55 (2014) 224-231.
- [63] C.-x. Miao, J.-j. Zheng, R.-j. Zhang, L. Cui, DEM modeling of pullout behavior of geogrid reinforced ballast: The effect of particle shape, *Computers and Geotechnics* 81 (2017) 249-261.
- [64] N.T. Ngo, B. Indraratna, C. Rujikiatkamjorn, M. Mahdi Biabani, Experimental and Discrete Element Modeling of Geocell-Stabilized Subballast Subjected to Cyclic Loading, *Journal of Geotechnical and Geoenvironmental Engineering* 142(4) (2016) 04015100.
- [65] Y. Liu, A. Deng, M. Jaksa, Three-dimensional modeling of geocell-reinforced straight and curved ballast embankments, *Computers and Geotechnics* 102 (2018) 53-65.
- [66] G. Jing, L. Qie, V. Markine, W. Jia, Polyurethane reinforced ballasted track: Review, innovation and challenge, *Construction and Building Materials* 208 (2019) 734-748.
- [67] J.-F. Ferrellec, R. Perales, V.-H. Nhu, M. Wone, G. Saussine, Analysis of compaction of railway ballast by different maintenance methods using DEM, *EPJ Web of Conferences, EDP Sciences*, 2017, p. 15032.
- [68] G. Saussine, E. Azéma, P. Gautier, R. Peyroux, F. Radjai, Numerical modeling of the tamping operation by Discrete Element Approach, *World Congress Rail Research*, 2008, pp. 1-9.
- [69] T. Zhou, B. Hu, J. Sun, Z. Liu, Discrete element method simulation of railway ballast compactness during tamping process, *Open Electrical & Electronic Engineering Journal* 7 (2013) 103-109.
- [70] R. Perales, G. Saussine, N. Milesi, F. Radjai, Numerical investigation of the tamping process, 9th World Congress on Railway Research, 2011.
- [71] X.J. Wang, Y.L. Chi, W. Li, T.Y. Zhou, X.L. Geng, The research of the numerical simulation on the granular ballast bed tamping, *Advanced Materials Research, Trans Tech Publ*, 2012, pp. 1395-1398.
- [72] T.M.P. Hoang, P. Alart, D. Dureisseix, G. Saussine, A domain decomposition method for granular dynamics using discrete elements and application to railway ballast, *Annals of Solid and Structural Mechanics* 2(2-4) (2011) 87-98.
- [73] D.S. Kim, S.H. Hwang, A. Kono, T. Matsushima, Evaluation of ballast compactness during the tamping process by using an image-based 3D discrete element method, *Proceedings of the Institution of Mechanical Engineers, Part F: Journal of Rail and Rapid Transit* 232(7) (2018) 0954409718754927.
- [74] H. Boler, Y. Qian, E. Tutumluer, Influence of Size and Shape Properties of Railroad Ballast on Aggregate Packing: Statistical Analysis, *Transportation Research Record: Journal of the Transportation Research Board* (2448) (2014) 94-104.
- [75] C. Coetzee, Calibration of the discrete element method and the effect of particle shape, *Powder Technology* 297 (2016) 50-70.
- [76] C. Coetzee, R. Nel, Calibration of discrete element properties and the modelling of packed rock beds, *Powder Technology* 264 (2014) 332-342.
- [77] B.s.p.B.E. British Standards Institution, *Aggregates for railway ballast*, British Standards Institution London, 2013.
- [78] T.P.M.o. Railways, *Railway Ballast, TB/T2140-2008*, China Railway Publishing House, Beijing, 2008.
- [79] A.R. Engineering, M.-o.-W. Association, *Manual for railway engineering*, American Railway Engineering and Maintenance-of-Way Association 2009.



- [80] M. Lu, G.R. McDowell, Discrete element modelling of railway ballast under triaxial conditions, *Geomechanics and Geoengineering* 3(4) (2008) 257-270.
- [81] Y. Guo, V. Markine, X. Zhang, W. Qiang, G. Jing, Image analysis for morphology, rheology and degradation study of railway ballast: A review, *Transportation Geotechnics* 18 (2019) 173-211.
- [82] C. Itasca, PFC (particle flow code in 2 and 3 dimensions), version 5.0 [User's manual], Minneapolis, 2014.
- [83] J. Kozicki, F.V. Donzé, YADE - OPEN DEM: an open - source software using a discrete element method to simulate granular material, *Engineering Computations* 26(7) (2009) 786-805.
- [84] H. Huang, Discrete element modeling of railroad ballast using imaging based aggregate morphology characterization, University of Illinois at Urbana-Champaign, 2010.
- [85] F. Dubois, M. Jean, M. Renouf, R. Mozul, A. Martin, M. Bagn  ris, Lmgc90, 10e colloque national en calcul des structures, 2011, p. Cl   USB.
- [86] R. Taghavi, Automatic clump generation based on mid-surface, *Proceedings, 2nd International FLAC/DEM Symposium*, Melbourne, 2011, pp. 791-797.
- [87] S.A. Galindo-Torres, J.D. Munoz, F. Alonso-Marroquin, Minkowski-Voronoi diagrams as a method to generate random packings of spheropolygons for the simulation of soils, *Physical review. E, Statistical, nonlinear, and soft matter physics* 82(5 Pt 2) (2010) 056713.
- [88] C. Ngamkhanong, S. Kaewunruen, C. Baniotopoulos, A review on modelling and monitoring of railway ballast, *Structural Monitoring and Maintenance* 4(3) (2017) 195-220.
- [89] S. Lobo-Guerrero, L.E. Vallejo, L.F. Vesga, Visualization of crushing evolution in granular materials under compression using DEM, *International Journal of Geomechanics* 6(3) (2006) 195-200.
- [90] S. Lobo-Guerrero, L.E. Vallejo, Influence of pile shape and pile interaction on the crushable behavior of granular materials around driven piles: DEM analyses, *Granular Matter* 9(3-4) (2007) 241-250.
- [91] S.N. Mahmud, D. Mishra, Development of 'Coarse to Fine Ratio' As a New Gradation Parameter to Study Ballast Packing, 2018 Joint Rail Conference, American Society of Mechanical Engineers, 2018, pp. V001T01A004-V001T01A004.
- [92] W. Song, B. Huang, X. Shu, J. Str  nsk  y, H. Wu, Interaction between Railroad Ballast and Sleeper: A DEM-FEM Approach, *International Journal of Geomechanics* 19(5) (2019) 04019030.
- [93] E. Alaei, A. Mahboubi, A discrete model for simulating shear strength and deformation behaviour of rockfill material, considering the particle breakage phenomenon, *Granular Matter* 14(6) (2012) 707-717.
- [94] B. Indraratna, T. Ngo, C. Rujikiatkamjorn, Performance of Ballast Influenced by Deformation and Degradation: Laboratory Testing and Numerical Modeling, *International Journal of Geomechanics* 20(1) (2019) 04019138.
- [95] W.L. Lim, G.R. McDowell, Discrete element modelling of railway ballast, *Granular Matter* 7(1) (2005) 19-29.
- [96] X. Zhang, C. Zhao, W. Zhai, DEM Analysis of Ballast Breakage Under Train Loads and Its Effect on Mechanical Behaviour of Railway Track, *Proceedings of the 7th International Conference on Discrete Element Methods* 188 (2017) 1323-1333.
- [97] C. Ergenzinger, R. Seifried, P. Eberhard, A discrete element model predicting the strength of ballast stones, *Computers & Structures* 108-109 (2012) 3-13.
- [98] C. Ergenzinger, R. Seifried, P. Eberhard, A Discrete Element Approach to Model Breakable Railway Ballast, *J Comput Nonlin Dyn* 7(4) (2012).
- [99] H. Gong, W. Song, B. Huang, X. Shu, B. Han, H. Wu, J. Zou, Direct shear properties of railway ballast mixed with tire derived aggregates: Experimental and numerical investigations, *Construction and Building Materials* 200 (2019) 465-473.
- [100] J.J. Kumara, K. Hayano, Y. Kikuchi, Deformation behaviour of gap-graded fouled ballast evaluated by a 3D discrete element method, *KSCIE Journal of Civil Engineering* 20(6) (2015) 2345-2354.
- [101] M. Stahl, H. Konietzky, Discrete element simulation of ballast and gravel under special consideration of grain-shape, grain-size and relative density, *Granular Matter* 13(4) (2010) 417-428.
- [102] W. Jia, V. Markine, Y. Guo, G. Jing, Experimental and numerical investigations on the shear behaviour of recycled railway ballast, *Construction and Building Materials* 217 (2019) 310-320.
- [103] J. Ferrellec, G. McDowell, Modelling realistic shape and particle inertia in DEM, *G  otechnique* 60(3) (2010) 227-232.
- [104] J.-F. Ferrellec, G.R. McDowell, A method to model realistic particle shape and inertia in DEM, *Granular Matter* 12(5) (2010) 459-467.
- [105] X. Zhang, C. Zhao, W. Zhai, Importance of load frequency in applying cyclic loads to investigate ballast deformation under high-speed train loads, *Soil Dynamics and Earthquake Engineering* 120 (2019) 28-38.
- [106] X. Wang, Y. Chi, Y. Ding, L. Gao, P. Xu, Y. Cao, B. Hua, Study on the simulation of the Railway Ballast under Cyclic Loading, *International Journal of Digital Content Technology and its Applications* 6(23) (2012) 642-650.
- [107] T.Y. Zhou, B. Hu, X.J. Wang, B. Yan, Discrete Element Method Analysis of Mechanical Properties of Railway Ballast during Tamping Process under Different Amplitude, *Applied Mechanics and Materials* 233 (2012) 224-227.
- [108] E. Tutumluer, H. Huang, Y. Hashash, J. Ghaboussi, AREMA gradations affecting ballast performance using discrete element modeling (DEM) approach, *Proceedings of the AREMA 2009 Annual Conference*, Chicago, Illinois, September, 2009, pp. 20-23.
- [109] E. Az  ma, F. Radjai, G. Saussine, Quasistatic rheology, force transmission and fabric properties of a packing of irregular polyhedral particles, *Mechanics of Materials* 41(6) (2009) 729-741.
- [110] G. Saussine, C. Cholet, P.E. Gautier, F. Dubois, C. Bohatier, J.J. Moreau, Modelling ballast behaviour under dynamic loading. Part 1: A 2D polygonal discrete element method approach, *Computer Methods in Applied Mechanics and Engineering* 195(19-22) (2006) 2841-2859.
- [111] N. Ouhbi, C. Voivret, G. Perrin, J.-N. Roux, Railway Ballast: Grain Shape Characterization to Study its Influence on the Mechanical Behaviour, *Procedia Engineering* 143 (2016) 1120-1127.
- [112] J. Eli  s, Simulation of railway ballast using crushable polyhedral particles, *Powder Technology* 264 (2014) 458-465.
- [113] S. Ji, S. Sun, Y. Yan, Discrete Element Modeling of Rock Materials with Dilated Polyhedral Elements, *Procedia Engineering* 102 (2015) 1793-1802.
- [114] J. Horabik, M. Molenda, Parameters and contact models for DEM simulations of agricultural granular materials: a review, *Biosystems Engineering* 147 (2016) 206-225.
- [115] C. Coetzee, Calibration of the discrete element method, *Powder Technology* 310 (2017) 104-142.
- [116] Y. Qian, S.J. Lee, E. Tutumluer, Y.M.A. Hashash, J. Ghaboussi, Role of Initial Particle Arrangement in Ballast Mechanical Behavior, *International Journal of Geomechanics* 18(3) (2018) 04017158.
- [117] B. Suhr, K. Six, Friction phenomena and their impact on the shear behaviour of granular material, *Computational particle mechanics* 4(1) (2017) 23-34.
- [118] S. Shao, Y. Yan, S. Ji, Combined Discrete-Finite Element Modeling of Ballasted Railway Track Under Cyclic Loading, *International Journal of Computational Methods* 14(05) (2017).

- [119] J. Irazábal, F. Salazar, E. Oñate, Numerical modelling of granular materials with spherical discrete particles and the bounded rolling friction model. Application to railway ballast, *Computers and Geotechnics* 85 (2017) 220-229.
- [120] Y. Cheng, M. Bolton, Y. Nakata, Crushing and plastic deformation of soils simulated using DEM, *Geotechnique* 54(2) (2004) 131-141.
- [121] O. Harireche, G.R. McDowell, Discrete element modelling of cyclic loading of crushable aggregates, *Granular Matter* 5(3) (2003) 147-151.
- [122] G. McDowell, O. Harireche, Discrete element modelling of yielding and normal compression of sand, *GEOTECHNIQUE* 52(4) (2002) 299-304.
- [123] W. Zhou, K. Xu, G. Ma, X.L. Chang, On the breakage function for constructing the fragment replacement modes, *Particuology* 44 (2019) 207-217.
- [124] S. Lobo-Guerrero, L.E. Vallejo, Discrete element method evaluation of granular crushing under direct shear test conditions, *Journal of Geotechnical and Geoenvironmental Engineering* 131(10) (2005) 1295-1300.
- [125] Y. Guo, V. Markine, W. Qiang, H. Zhang, G. Jing, Effects of crumb rubber size and percentage on degradation reduction of railway ballast, *Construction and Building Materials* 212 (2019) 210-224.
- [126] R.D. Mindlin, Elastic spheres in contact under varying oblique forces, *J. Applied Mech.* 20 (1953) 327-344.
- [127] L. Li, W. Liu, M. Ma, G. Jing, W. Liu, Research on the dynamic behaviour of the railway ballast assembly subject to the low loading condition based on a tridimensional DEM-FDM coupled approach, *Construction and Building Materials* 218 (2019) 135-149.
- [128] J. Harkness, Potential particles for the modelling of interlocking media in three dimensions, *International Journal for Numerical Methods in Engineering* 80(12) (2009) 1573-1594.
- [129] I. Deiros Quintanilla, Multi-scale study of the degradation of railway ballast, Grenoble Alpes, 2018.
- [130] J.J. Moreau, Some numerical methods in multibody dynamics: application to granular materials, (1994).
- [131] T.M.P. Hoang, G. Saussine, D. Dureisseix, P. Alart, Behaviour of a portion of railway track under maintenance operation, 9th World Congress on Railway Research–WCRR2011, Lille, France, 2011.
- [132] S. Zhao, X. Zhou, W. Liu, Discrete element simulations of direct shear tests with particle angularity effect, *Granular Matter* 17(6) (2015) 793-806.
- [133] L. Wang, J.-Y. Park, Y. Fu, Representation of real particles for DEM simulation using X-ray tomography, *Construction and Building Materials* 21(2) (2007) 338-346.
- [134] S.P.K. Kodicherla, G. Gong, Z.X. Yang, K. Krabbenhoft, L. Fan, C.K.S. Moy, S. Wilkinson, The influence of particle elongations on direct shear behaviour of granular materials using DEM, *Granular Matter* 21(4) (2019).
- [135] Y. Liu, R. Gao, J. Chen, Exploring the influence of sphericity on the mechanical behaviors of ballast particles subjected to direct shear, *Granular Matter* 21(4) (2019).
- [136] G. Jing, P. Aela, Review of the lateral resistance of ballasted tracks, *Proceedings of the Institution of Mechanical Engineers, Part F: Journal of Rail and Rapid Transit* (2019) 095440971986635.
- [137] K. Senetakis, C.S. Sandeep, Experimental study of sand grains behavior at their contacts with force- and displacement-controlled sliding tests, *Underground Space* 2(1) (2017) 38-44.
- [138] L. Xin, V. Markine, I. Shevtsov, Numerical procedure for fatigue life prediction for railway turnout crossings using explicit finite element approach, *Wear* 366 (2016) 167-179.
- [139] C. Wan, V. Markine, I. Shevtsov, Improvement of vehicle–turnout interaction by optimising the shape of crossing nose, *Vehicle System Dynamics* 52(11) (2014) 1517-1540.
- [140] P. Wang, J. Xu, K. Xie, R. Chen, Numerical simulation of rail profiles evolution in the switch panel of a railway turnout, *Wear* 366 (2016) 105-115.
- [141] C. Shi, C. Zhao, X. Zhang, Y. Guo, Coupled discrete-continuum approach for railway ballast track and subgrade macro-meso analysis, *International Journal of Pavement Engineering* (2020) 1-16.
- [142] C. Shi, C. Zhao, X. Zhang, A. Andersson, Analysis on dynamic performance of different track transition forms using the discrete element/finite difference hybrid method, *Computers & Structures* 230 (2020) 106187.
- [143] M. Jiang, Z. Shen, J. Wang, A novel three-dimensional contact model for granulates incorporating rolling and twisting resistances, *Computers and Geotechnics* 65 (2015) 147-163.